

The eROSITA Final Equatorial Depth Survey (eFEDS):

X-ray emission around star-forming and quiescent galaxies at $0.05 < z < 0.3$

Johan Comparat^{1*}, Nhut Truong², Andrea Merloni¹, Annalisa Pillepich², Gabriele Ponti^{3,1}, Simon Driver^{4,5}, Sabine Bellstedt⁴, Joe Liske⁶, James Aird^{7,8}, Marcus Brüggen⁶, Esra Bulbul¹, Luke Davies⁴, Justo Antonio González Villalba¹, Antonis Georgakakis⁹, Frank Haberl¹, Teng Liu¹, Chandreyee Maitra¹, Kirpal Nandra¹, Paola Popesso¹⁰, Peter Predehl¹, Aaron Robotham⁴, Mara Salvato¹, Jessica E. Thorne⁴, Yi Zhang¹

¹ Max-Planck-Institut für extraterrestrische Physik (MPE), Gießenbachstraße 1, D-85748 Garching bei München, Germany

² Max-Planck-Institut für Astronomie, Königstuhl 17, D-69117 Heidelberg, Germany

³ INAF-Osservatorio Astronomico di Brera, Via E. Bianchi 46, I-23807 Merate (LC), Italy

⁴ International Centre for Radio Astronomy Research (ICRAR), University of Western Australia, Perth, Western Australia, Australia;

⁵ International Space Centre (ISC), University of Western Australia, Perth, Western Australia, Australia

⁶ Hamburger Sternwarte, University of Hamburg, Gojenbergsweg 112, D-21029 Hamburg, Germany

⁷ Institute for Astronomy, Royal Observatory, University of Edinburgh, Edinburgh EH9 3HJ, UK

⁸ School of Physics & Astronomy, University of Leicester, University Road, Leicester LE1 7RJ, UK

⁹ Institute for Astronomy and Astrophysics, National Observatory of Athens, V. Paulou & I. Metaxa, 11532, Greece

¹⁰ European Southern Observatory, D-85748 Garching bei München, Germany

January 17, 2022

ABSTRACT

Aims. The circum-galactic medium (CGM) plays an important role in galaxy evolution as the main interface between the star-forming body of galaxies and the surrounding cosmic network of in- and out-flowing matter. In this work, we aim at characterizing the hot phase of the CGM in a large sample of galaxies using recent soft X-ray observations made by *SRG/eROSITA*.

Methods. We stack X-ray events from the ‘eROSITA Final Equatorial Depth Survey’ (eFEDS) around central galaxies in the 9hr field of the ‘Galaxy and Mass Assembly’ (GAMA) survey to construct radially projected X-ray luminosity profiles in the 0.5–2 keV rest frame energy band as a function of their stellar mass and specific star formation rate. We consider samples of quiescent (star-forming) galaxies in the stellar mass range $2 \times 10^{10} - 10^{12} M_{\odot}$ ($3 \times 10^9 - 6 \times 10^{11} M_{\odot}$).

Results. For quiescent galaxies, the X-ray profiles are clearly extended throughout the available mass range; however, the measured profile is likely biased high due to projection effects, as these galaxies tend to live in dense and hot environments. For the most massive star forming samples ($\geq 10^{11} M_{\odot}$), there is a hint of detection of extended emission. On the other hand, for star-forming galaxies with $< 10^{11} M_{\odot}$ the X-ray stacked profiles are compatible with unresolved sources and consistent with the expected emission from faint active galactic nuclei (AGN) and X-ray binaries. We measure for the first time the mean relation between average X-ray luminosity and stellar mass separately for quiescent and star-forming galaxies. We find that the relation is different for the two galaxy populations: high-mass ($\geq 10^{11} M_{\odot}$) star-forming or quiescent galaxies follow the expected scaling of virialized hot haloes, while lower mass star-forming galaxies show a less prominent luminosity and a weaker dependence on stellar mass, consistent with empirical models of the population of weak AGN. When comparing our results with state-of-the-art numerical simulations (IllustrisTNG and EAGLE), we find an overall consistency on the average emission on large (> 80 kpc) scales at masses $\geq 10^{11} M_{\odot}$, but disagreement on the small scales, where brighter than observed compact cores are predicted. The simulations also do not predict the clear differentiation that we observe between quiescent and star-forming galaxies in our samples.

Conclusions. This is a stepping stone towards a more profound understanding of the hot phase of the CGM, which holds a key role in the regulation of star formation. Future analysis using eROSITA all-sky survey data, combined with future generation galaxy evolution surveys, shall provide much enhanced quantitative measures and mappings of the circum-galactic medium and its hot phase(s).

Key words. X-ray, galaxies, circum-galactic medium

1. Introduction

A precise description of the different phases of the cosmic gas, from the inter-galactic (IGM) to the circum-galactic medium (CGM) around galaxies, is the missing piece to establish an accurate baryon budget in the Universe (Tumlinson et al. 2017; Driver 2021). The physical properties of the warm-hot component of the inter-galactic and halo gas, supposedly comprising

40% of the baryons, remains until now vastly unconstrained. In that regard, L^* galaxies hosted by $10^{12} M_{\odot}$ haloes, where most of the stars and metals are formed (Moster et al. 2018; Behroozi et al. 2019), are of great interest. Soft X-ray observations represent a particularly useful tool to investigate the properties of the halo gas around galaxies, as the warm-hot phase itself should reach virial temperatures such that most of the emission emerges in this band (Fukugita & Peebles 2004, 2006).

* E-mail: comparat@mpe.mpg.de

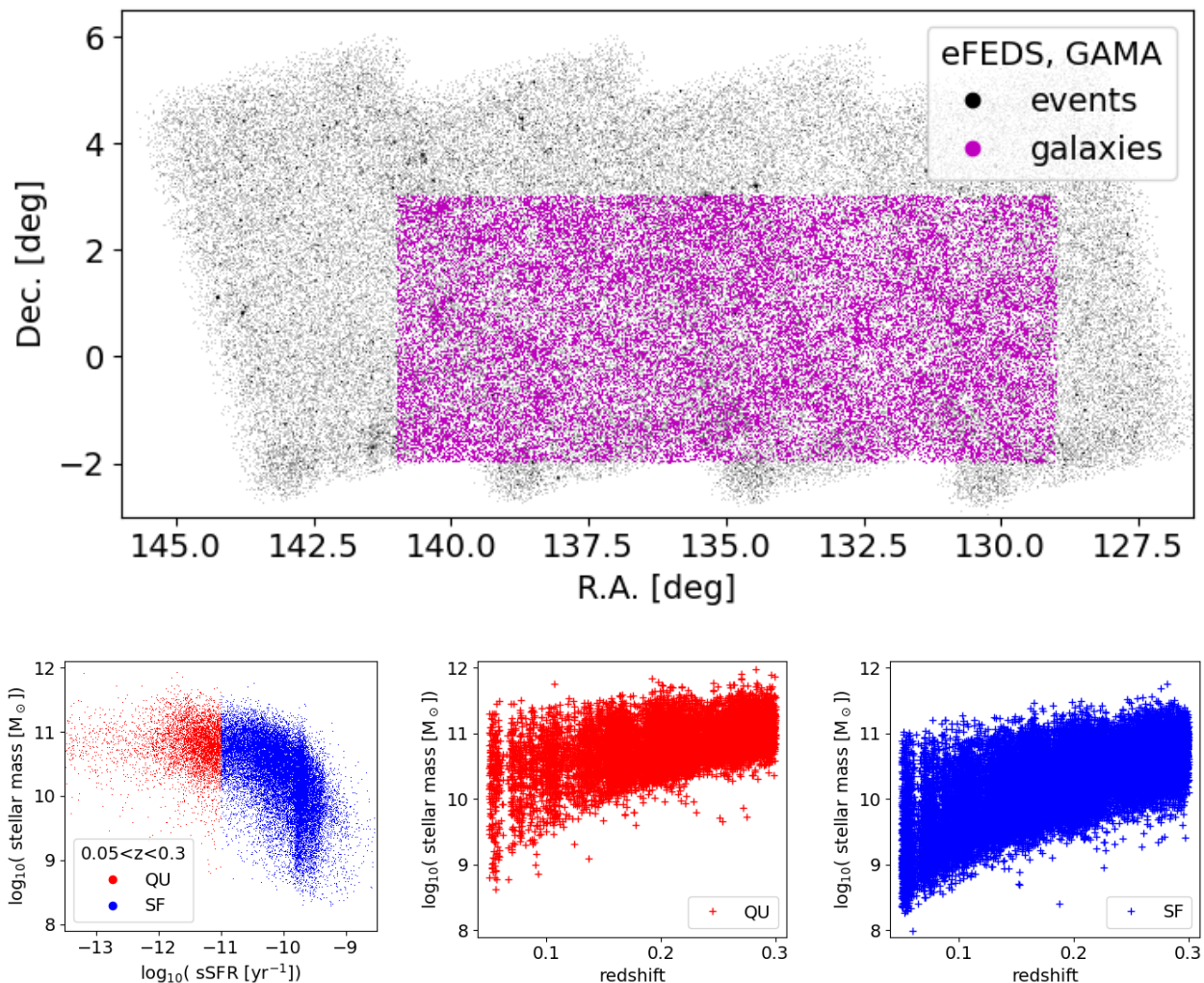


Fig. 1. Figures describing the set of central galaxies used in this work. **Top.** Sky coverage of eFEDS data (grey points) and GAMA galaxies (magenta). **Bottom panels.** The split between star-forming and quiescent galaxies is illustrated on the leftmost panel. It is done via a boundary at $\log_{10}(sSFR) = -11$. Stellar mass ($\log_{10}(M/M_{\odot})$) vs. redshift for the set of quiescent (middle) and star-forming (right) galaxies available in the GAMA 9h field.

In fact, hot and X-ray emitting haloes have been observed around *individual* or small samples of galaxies in the past. This has been generally achieved for early-type massive galaxies (e.g. [Goulding et al. 2016](#); [Bregman et al. 2018](#)). The detection of X-ray emitting atmospheres around disk, star-forming galaxies is rare and limited to small samples of galaxies more massive than $\sim 10^{11}M_{\odot}$ (e.g. [Bogdán et al. 2013a,b, 2017](#); [Anderson et al. 2016](#); [Li et al. 2016](#)).

[Anderson et al. \(2015\)](#) stacked X-ray photons from the ROSAT all-sky survey around 250,000 massive galaxies from the Sloan Digital Sky Survey that are central within their dark-matter haloes. They reported a strong correlation between the mean X-ray luminosity of the volume-filling gas in the CGM (i.e. in the range $(0.15 - 1) \times R_{500c}^1$) and the galaxy stellar mass, in the stellar mass range $\log M^*/M_{\odot} = 10.8 - 12$. However, due to the limited spatial resolution and the bright flux limit of ROSAT, it was not possible to firmly detect an X-ray emission signal from the CGM of Milky Way-mass (MW) galaxies and below ($\lesssim 10^{10.7}M_{\odot}$).

¹ R_{500c} is the radius at which the density of the dark matter halo is 500 times the critical density of the Universe at the redshift of the system.

From a theoretical perspective, the extended, soft X-ray emission from the gaseous atmospheres of massive haloes has been predicted by galaxy formation models in the full cosmological context since the analytical models of [White & Frenk \(1991\)](#). This has been confirmed, albeit with overall lower luminosity than previously expected, by the results of cosmological hydro-dynamical simulations, also around disk and MW-mass galaxies (e.g. [Crain et al. 2010](#); [Bogdán et al. 2015](#); [Kelly et al. 2021](#), with the GIMIC, Illustris and EAGLE simulations, respectively). These works have shown that such X-ray emission is sensitive to the unfolding and the interplay of star formation, feedback and cooling processes, which simultaneously can remove low-entropy gas by star formation, heat up the halo gas via energy injections, but can also redistribute the gas via outflows, making gaseous haloes dilute. Recently, [Truong et al. \(2020\)](#) and [Oppenheimer et al. \(2020\)](#) have shown that the state-of-the-art cosmological galaxy simulations IllustrisTNG and EAGLE both predict an X-ray luminosity dichotomy at $z \sim 0$: at the transitional stellar mass regime of $10^{10.5-11}M_{\odot}$, simulated star-forming galaxies in fact exhibit somewhat *higher* soft X-ray luminosity from the volume-filling gas within and around

them than quiescent galaxies of the same mass, all the way out to galactocentric distances of ~ 200 kpc. Despite the differences in feedback processes implemented therein, this has been shown to be a direct manifestation of the quenching mechanism in the simulations, with the reduction of the gas mass within the haloes due to super massive black hole (SMBH) driven outflows. Clearly, robust statistical constraints on the properties of the X-ray emitting gas from large samples of galaxies in this transitional mass regime may hold the key to further improve our understanding of the complex physical processes shaping up the gaseous atmosphere of their haloes.

In this article, we bridge the gap between past studies by attempting to measure the faint, extended X-ray emission, i.e. the so-called hot phase of the CGM, surrounding central galaxies over a wide stellar mass range ($\approx 10^{9.6-11.8} M_{\odot}$) by stacking *SRG*/eROSITA data, taking advantage of its high sensitivity in soft X-rays, moderate spatial resolution, large grasp and stable background (Predehl et al. 2021). In order to do that, we use data from the eROSITA performance verification eFEDS field (Brunner et al. 2021), a 140 deg^2 survey that partly overlaps with a highly complete spectroscopic sample of low redshift ($0.05 < z < 0.3$) galaxies (GAMA, Sloan Digital Sky Survey (SDSS), Liske et al. 2015; Ahumada et al. 2020). We can hence stack X-ray data around galaxies in different bins of stellar mass, and distinguish between star-forming and quiescent ones.

A brief description of the data used is presented in Sect. 2. The method, close to that adopted by Anderson et al. (2015), is described in detail in Sect. 3. In Sect. 4, we discuss the measurements obtained, while in Sect. 5 we compare the measurements with hydro-dynamical simulations. We discuss possible implications of our results for galaxy evolution in Sect. 6.

2. Data

2.1. eROSITA eFEDS data

We use for this work the public Early Data Release (EDR) eROSITA event file of the eFEDS field (Brunner et al. 2021)². It contains about 11 million events (X-ray photons), detected by eROSITA, over the 140 deg^2 area of the eFEDS Performance Verification survey. Each photon is assigned an exposure time using the vignetting corrected exposure map. Photons close to detected sources in the source catalogue are flagged (see details in Sect. 3.2). These sources are catalogued as point-like or extended based on their X-ray morphology (Brunner et al. 2021), and they are further classified (e.g. galactic, active galactic nuclei, individual galaxies at redshift $z < 0.05$, galaxy group and clusters) using multi-wavelength information (Salvato et al. 2021; Vulic et al. 2021; Liu A et al. 2021; Liu T et al. 2021; Bulbul et al. 2021).

2.2. GAMA galaxy catalogue

From the GAMA survey (Liske et al. 2015), we retrieve in the 9hr field (SpectCatv27 and $NQ > 2$), about 40,000 galaxies with a spectroscopic redshift in the range $0.05 \leq z \leq 0.3$ with measured stellar mass and specific star formation rate (sSFR) from Bellstedt et al. (2020, 2021). They are derived using spectral energy distribution fitting (Robotham et al. 2020). They adopt a Chabrier initial mass function and SFRs are averaged over 100 Myr. Stellar masses are output in unit of solar mass (M_{\odot}) and

specific star formation rate in year inverse (yr^{-1}). The exact selection of galaxies is detailed in Sect. 3.1.

We note that the GAMA galaxy sample only covers a fraction of the eFEDS area 60 deg^2 out of 140 deg^2 , see Fig. 1 top panel. Necessarily, we limit our X-ray analysis to this 60 deg^2 area.

3. Method

By stacking large data sets the noise decreases and features with weak signal may be unveiled (e.g. Zhu et al. 2015; Comparat et al. 2020b; Wolf et al. 2020). To do so, we stack X-ray events around central galaxies with known spectroscopic redshift (Sect. 3.1), after masking detected X-ray sources (Sect. 3.2).

We keep track of the angular distance between the detected X-ray event and the galaxy (and its redshift) to build radial profiles. We record the event energies to build X-ray spectra. We obtain a data cube where angular coordinates are converted to proper distance (angle averaged) radii and the energy (or wavelength) vector is shifted to the galaxy redshift. The stacking procedure is described in detail in Sect. 3.3.

In the measurement process, control on two systematic features is key: the emission of the background and the instrumental signatures. To simplify our analysis, and in light of the expected spectral energy distribution of the signal we are interested in, we focus here on the rest-frame energy range between 0.5 and 2 keV. In doing so, we only consider the energy range where the background emission is dominated by the well-understood diffuse emission of the Milky Way and by the Cosmic X-ray Background (e.g. Predehl et al. 2021; Liu T et al. 2021, Ponti et al. in preparation), while the contribution of the particle (un-vignetted) background is negligible. Moreover, we avoid the complex response of the lowest energy range (below ~ 0.4 keV in the observed frame) where both detector noise and the effects of the light leak on the TM5 and TM7 (see Predehl et al. 2021) could introduce yet un-calibrated systematic effects. As in Brunner et al. (2021), we select good events from nominal field of view, exclude bad pixels, and keep events with $\text{PATTERN} \leq 15$, which includes single, double, triple, and quadruple events. Also, given the relatively low signal to noise ratio (SNR) achieved from relatively small galaxy samples, we only focus our attention on broad-band photometric measurements. Work is ongoing on the calibration of the low-energy response of eROSITA, and future works will explore the possibility of stacked spectral analysis also in the 0.15–0.4 keV observed-frame energy range.

We apply a bootstrap procedure to reliably estimate the mean expected background and its variance (Sect. 3.4). Finally, we estimate the spatial extent of the point source profile using an empirical point spread function (PSF) model based on the detected point sources in the same eFEDS field, as we describe in Sect. 3.5.

3.1. Selecting galaxies

We select central galaxies, most massive within their host dark matter halo, similarly to Planck Collaboration et al. (2013). For each GAMA galaxy, we infer its host halo mass and corresponding virial radius with the stellar to halo mass relation from Moster et al. (2013). If a galaxy lies within twice the virial radius of a galaxy of higher stellar mass, it is considered as a satellite and removed from the sample. The choice of two times the virial radius is a conservative one, to account for the scatter in the stellar mass to halo mass relation. We treat separately the X-ray detected eFEDS clusters (Liu A et al. 2021) for which we

² <https://erosita.mpe.mpg.de/edr>

Table 1. Samples considered in the analysis.

Sample name	stellar mass		N_g	Average	
	min	max		\bar{M}	\bar{z}
ALL_M10.7	10.4	11.0	16142	10.7	0.22
Fixed stellar mass selection					
QU_M10.7	10.0	11.0	7267	10.72	0.2
SF_M10.7	10.4	11.0	9846	10.66	0.23
Quiescent galaxies					
QU_M11.71	11.616	11.973	50	11.71	0.27
QU_M11.58	11.556	11.616	50	11.58	0.27
QU_M11.54	11.523	11.556	50	11.54	0.26
QU_M11.35	11.306	11.41	400	11.35	0.25
QU_M11.2	11.138	11.269	1002	11.2	0.25
QU_M11.04	10.961	11.138	2000	11.04	0.24
QU_M10.88	10.806	10.961	1999	10.88	0.23
QU_M10.73	10.641	10.806	1999	10.73	0.21
QU_M10.53	10.362	10.641	2000	10.53	0.19
star-forming galaxies					
SF_M11.25	11.17	11.754	400	11.25	0.27
SF_M11.12	11.079	11.17	400	11.12	0.27
SF_M11.05	11.027	11.079	401	11.05	0.26
SF_M10.99	10.943	11.051	1000	10.99	0.26
SF_M10.9	10.861	10.943	1001	10.9	0.25
SF_M10.86	10.795	10.943	2000	10.86	0.25
SF_M10.74	10.68	10.795	2000	10.74	0.24
SF_M10.63	10.574	10.68	2002	10.63	0.23
SF_M10.52	10.467	10.574	1998	10.52	0.22
SF_M10.41	10.358	10.467	2001	10.41	0.21
SF_M10.3	10.241	10.358	2000	10.3	0.2
SF_M10.18	10.108	10.241	2001	10.18	0.19
SF_M10.03	9.947	10.108	1998	10.03	0.18
SF_M9.86	9.761	9.947	2000	9.86	0.16
SF_M9.64	9.491	9.761	2000	9.64	0.14

Notes. SF stands for Star-Forming and QU for Quiescent. We report the number of galaxies present in each sample (N_g) and their average properties: stellar mass (\bar{M}) and redshift (\bar{z}).

have individual measurements of R_{500c} (Bahar et al. 2021). For them, we only remove satellites falling within one virial radius, taken as $R_{500c}/0.7$. After this filtering, $\sim 10\%$ of the galaxies are removed, and we obtain a sample of 35,521 central galaxies. Thanks to the high completeness ($\sim 98\%$) of the GAMA sample, the sample of central galaxies should be also highly complete. We discuss limitations due to our sample definition in Sect. 6.2

We use the reported stellar masses and specific star formation rates to create sub-samples of the galaxy population. In order to examine trends, we split the population into star-forming and quiescent galaxies assuming a boundary fixed at $\log_{10}(sSFR) = -11$ (see discussion by Davies et al. 2019; Thorne et al. 2021). For this study, in which we stack around a large number of galaxies, the exact boundary definition should have a minor impact. Figure 1 shows the distribution of galaxies in the redshift range of interest in the mass-sSFR plane.

To compare the star-forming and quiescent samples at fixed stellar mass, we first adopt a stellar mass selection to obtain two samples with the same mean stellar mass, different sSFR and a similar total number of galaxies. By taking objects within $10 < \log_{10} M^* < 11$ for the quiescent and $10.4 < \log_{10} M^* < 11$ for the star-forming galaxies, we obtain for both a mean stellar mass of $5 \times 10^{10} M_{\odot}$ with a set of 7,267 and 9,846 galaxies, respectively.

Each population, star-forming or quiescent, is then split in a number of non-overlapping stellar mass sub-samples (see Table 1). As stellar mass correlates with X-ray luminosity (Anderson et al. 2015), to obtain a similar signal to noise from the various sub-samples, fewer galaxies are needed at higher mass than at lower mass. So, we create sub-samples of ~ 2000 at the low mass end, then 1000, 400 and finally 50 galaxies at the high mass end. Table 1 details the exact number of galaxies present in each subclass. There, we also report the mean redshift and mean stellar mass for each sub-sample defined in this way.

3.2. Masking approaches and possible sources of contamination

As we are after faint diffuse emission, it is vital to remove (mask out) as much as possible all sources of contamination produced by un-resolved emission from compact sources within galaxies. In this work, we investigate four possible masking schemes (see Table 2):

- (i) ‘ALL’ mask: all detected X-ray sources are masked;
- (ii) ‘M1’ mask: all detected sources are masked except for those associated with a cluster or a group in the same redshift range as the GAMA galaxies, as identified by Liu A et al. (2021) or by Bulbul et al. (2021), taking CLUSTER_CLASS = 4 or 5, (see Salvato et al. 2021);
- (iii) ‘M2’ mask: all detected sources are masked except for point sources in the redshift range of interest associated by Salvato et al. (2021) to a GAMA galaxy;
- (iv) ‘M3’ mask: all detected sources are masked except for those unmasked by the M1 or M2 mask. The signal obtained is to be interpreted as the sum of all emitting entities: active galactic nuclei (AGN), X-ray binaries (XRB), hot gas, augmented by systematic projection effects.

The masking radius for each detected source (with a detection likelihood larger than 6) is its radius of maximum signal to noise, as determined while extracting the X-ray spectrum of each source (Liu T et al. 2021), augmented by 40 per cent. By doing so, we make sure there is no remaining correlation between the set of events outside of the mask and the source catalogue (Comparat et al. in prep.). The optimal masking radius, derived with limited statistics on eFEDS data, suffers from uncertainties; augmenting the masking radius by 30% or 50% is also reasonable and corresponds to masking 2 per cent less or more events, as shown in Table 2. This uncertainty on the total number of events directly impacts the normalization of the profiles estimated. To account for this, we add a systematic 2% uncertainty on the background luminosity density (our normalization), see Sect. 3.4.

We use the sensitivity map to generate a catalogue of random points following Georgakakis et al. (2008). Armed with this, we estimate that masking all X-ray sources removes 27.13% of the events (and 6.9% of the area) in the 0.5–2 keV band. The least stringent mask, ‘M3’, removes 24.14% of the events (and 6.1% of the area; see Table 2).

The baseline mask used in this study is the M1 mask: all sources are masked except for sources identified as galaxy groups or clusters at $0.05 \leq z \leq 0.3$. Indeed, masking these extended sources would bias low the X-ray profiles of high mass galaxies. The other masks enable us the investigation of systematic effects due to the masking procedure. In particular, we will present a detailed comparison with the results from the M3 mask, which include in addition the emission from all the GAMA sources detected by eROSITA as point sources. These galaxies

Table 2. Fraction of events masked

mask name	fraction of masked events		masked area fraction
	% augmentation of masking radius		
	40	(30, 50)	a_{mask}
ALL	0.2713	(0.2565, 0.2863)	0.069
M1	0.259	(0.245, 0.2732)	0.066
M2	0.2542	(0.2394, 0.2696)	0.065
M3	0.2414	(0.2275, 0.256)	0.061

Notes. Fraction of masked events for a radius of maximum signal to noise augmented by 30 to 50%. 40% is the baseline used in the analysis. Masks are ordered by decreasing masked fraction. The percentage of area masked corresponding to the 40% baseline is given in the last column.

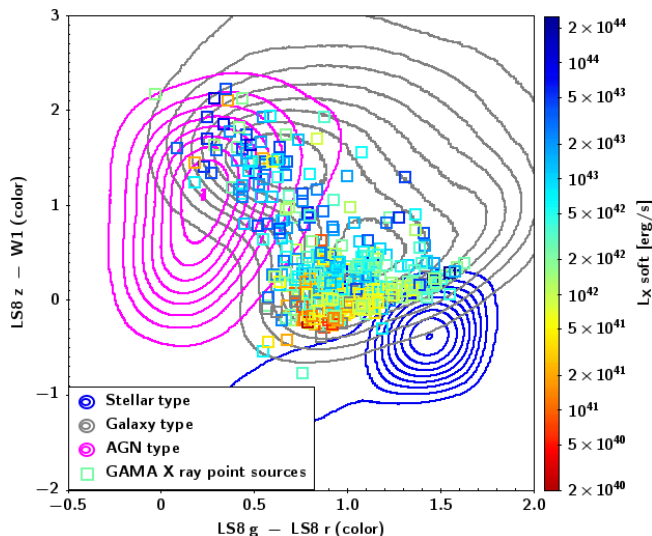


Fig. 2. Color-color diagram of the counterparts to all X-ray point sources detected in eFEDS. Type 1 (un-obscured) AGN and Quasar (QSO) occupy the left part of the plot (pink contours), the stars the bottom right corner (blue contour) and galaxy-like spectral energy distribution (characteristic of obscured AGN and passive galaxies) are in between (grey contour); see Salvato et al. (2021) for more details. The X-ray detected sources among the GAMA galaxy population are shown as empty squares, color-coded by their soft X-ray luminosity. They sample well the low- z QSO and the galaxy loci. By using the M3 mask, which includes these sources, one clearly adds to the stacks emission coming from luminous and moderately luminous AGN.

associated to an X-ray detected point source in the eFEDS catalog span the optical – near infra-red color-color plane in a similar fashion as the complete X-ray sample in this redshift range, see Fig. 2. Using the classification based on the broad band spectral energy distribution fits from Salvato et al. (2021) we note that GAMA galaxies matched to X-ray sources sample both the un-obscured AGN locus and, predominantly, the galaxy locus.

Below, we discuss in more detail the possible contamination due to faint, undetected AGN or XRB, and the relationship with the alternative masking approaches.

3.2.1. Expected AGN signal

AGN X-ray emission is produced in a very compact (fraction of a milli-parsec) region close to the central supermassive black holes in the nuclei of galaxies, and thus represent a contamination to the CGM signal. To ease the interpretation of the stacked profiles, then, we would ideally remove as many active galaxies

from the sample as possible. Given the moderate angular resolution of eROSITA, however, this step is far from straightforward.

In order to assess our ability to remove AGN contaminants, we discuss first the completeness of GAMA towards X-ray AGN detected by eROSITA.

Within the eFEDS X-ray point-source catalogue, considering all those counterparts in the GAMA 9h field and in the redshift range $0.05 < z < 0.3$, using either spectroscopic or high-quality photometric redshifts (see Salvato et al. 2021), we obtain 619 X-ray sources. Of these, 474 (76.6%) are matched within $2''$ to a galaxy present in the GAMA catalogue. When limiting the X-ray catalogue to sources with an LS8 magnitude $r < 19.8$ (19), similar to the magnitude limit used in GAMA, 88.8% (90.2%) are matched to GAMA galaxies. This implies that, at the magnitude limit of GAMA, the galaxy catalog is nearly complete in terms of the bright X-ray point-source population detected in eFEDS. In turn, this is consistent with the known spectroscopic completeness achieved by GAMA at these magnitude limits, and with the GAMA target selection, which uses a combination of criteria to exclude stars, while keeping compact galaxies and Quasar (QSO) (Baldry et al. 2010). The remaining bright unmatched X-ray sources are typically fainter in the optical than the GAMA limit; those are always masked out in the stacks.

The point-sources X-ray flux limit of eFEDS; $\sim 6.5 \times 10^{-15}$ erg s $^{-1}$ cm $^{-2}$ in the 0.5–2 keV band (Brunner et al. 2021) corresponds, at the redshift of the GAMA sources we are interested in, to a rest-frame luminosity between about 5×10^{40} and 2×10^{42} erg s $^{-1}$. Removing photons around all detected point-like X-ray sources that are matched to a GAMA galaxy (M1 mask) thus removes all the bright AGN from the sample. However, within the GAMA galaxy catalogues, a fraction of galaxies are expected to host faint AGN, which remain undetected given the eROSITA/eFEDS flux limit. Aird et al. (in preparation) study the point source emission emerging from GAMA galaxy stacks (as a function of stellar mass and redshift) to determine the faint end of the AGN X-ray luminosity function. They measure and model the average luminosity and the fraction of galaxies hosting an X-ray AGN. For a stellar mass ($\log_{10}(M^*/[M_{\odot}])$) of 9.75 (10.75, 11.75), they find an average luminosity of $\log_{10}(L_X/[erg\ s^{-1}]) \approx 40, (41, 42)$ and an occupation fraction of 0.1% (1%, 10%).

We further discuss AGN contamination and compare these figures with our observations in Sect. 6.1.

3.2.2. Expected X-ray binary signal

X-ray binaries, end-points of stellar evolution, are known contributors to the total X-ray luminosity of a galaxy (Tauris & van den Heuvel 2006). They are typically spatially distributed following the stellar light, and therefore their emission would be unresolved by eROSITA at the redshift of interest here.

We evaluate the possible contribution from these (unresolved) X-ray binaries, by taking advantage of the known scaling relation between their total X-ray luminosity and their host galaxy properties. In particular, in order to predict the X-ray luminosity of X-ray binaries (XRB) emitted by each galaxy, we use an analytical model based on Lehmer et al. (2016) and Aird et al. (2017). They measured the dependence of the total XRB luminosity (in the 2–10 keV energy band) on redshift, galaxy stellar mass and star formation rate. To make sure our prediction is conservative, we use the Aird et al. (2017) model, which produces a 10-20% brighter XRB luminosity for a given galaxy property. We use model 5 with parameters given in their Table 3 to predict the X-ray luminosity in the band 2-10 keV. We prop-

agate the uncertainties from Table 3 to the prediction. We then convert (multiplication by 0.56) the luminosity to the 0.5–2 keV band assuming an absorbed (with n_H column density set at mean value of the field $4 \times 10^{20} \text{ cm}^{-2}$) power-law with a photon index of 1.8 (as suggested by [Basu-Zych et al. 2020](#)).

3.3. Stacking procedure

We assume a Flat Λ CDM cosmology with $H_0 = 67.74 \text{ km s}^{-1} \text{ Mpc}^{-1}$, $\Omega_m(z=0) = 0.3089$ ([Planck Collaboration et al. 2016](#)).

Each galaxy is characterized by its position on the sky and its redshift, as well as properties of its stellar population (mass, specific star formation rate). We denote a galaxy with the vector \mathbf{G} defined as

$$\mathbf{G} = (G_{RA}, G_{Dec}, G_z, G_M, G_{SSFR}). \quad (1)$$

Given a galaxy, we retrieve all the events within the angle subtended by 3 Mpc at the galaxy redshift. We construct a ‘cube’ of event surrounding each galaxy. For each event, we compute a rest-frame energy by multiplying the energy by one plus the galaxy redshift: $E_{rf} = E_{obs} \times (1 + G_z)$. So, each eROSITA event is characterized by the following vector: its position on the sky (R.A., Dec.), its rest frame and observed energy, the corresponding galaxy redshift, the exposure time and the on-axis telescope effective area as a function of energy (ARF) at the observed energy, the projected distance (R_p) in proper kpc to the galaxy. We denote an event with the vector \mathbf{E} defined as

$$\mathbf{E} = (\text{R.A.}, \text{Dec.}, E_{obs}, E_{rf}, G_z, t_{exp}, \text{ARF}(E_{obs}), R_p). \quad (2)$$

The exposure times are obtained from the vignettted exposure map ([Brunner et al. 2021](#)). Using the (angular) projected distance induces projection effects which we discuss in Sect. 6.2.

We repeat this procedure with sets of random locations in the field, replacing the galaxy positions with randomly drawn positions in the same area of the sky, taking advantage of the relatively uniform exposure of the eFEDS field ([Brunner et al. 2021](#)).

Finally, in order to derive accurate correction to the measured fluxes for masking and boundary effects (due to the reduction of projected area), we repeat the above procedure with another two sets of random events. A first set of random events samples uniformly the area covered in the GAMA field (RE_G). A second set of events samples uniformly the GAMA area and an additional 1.5 degree wide stripe around (RE_W). This will allow us to account for boundary-effects in the area normalization of the background counts (see Sect. 3.4).

We apply each selection defined in Table 1 to the galaxy sample and to the random galaxy samples. We concatenate the event sets obtained. For each galaxy sample, we obtain five ‘cubes’ of events: galaxies-events (data cube), random galaxies-events (random cube), point-source galaxies-events (point source cube, detailed in Sect. 3.5), galaxies- RE_G cube, galaxies- RE_W cube.

Each event in any of the cubes is weighted by the following function:

$$w_i = \frac{A_{\text{corr}}(r) \times 1.602177 \times 10^{-12} E_{rf} 4\pi d_L^2(G_z)}{\text{ARF}(E_{obs}) t_{exp} \times N_g}, \quad (3)$$

where N_g is the number of galaxies in a sample (given in Table 1). A_{corr} is the area correction term, which accounts for both boundary effects and masks:

$$A_{\text{corr}}(r) = 1 + \frac{RE_W(r)}{RE_G(r)} + a_{\text{mask}}, \quad (4)$$

where r is the proper projected separation in kpc. For the full sample, the correction $\frac{RE_W(r)}{RE_G(r)}$ is 0.5% at 100 kpc, 1% at 300 kpc, 2.5% at 1000 kpc and 5% at 2 Mpc. For the M1 mask, $a_{\text{mask}} = 0.066$, for other masks, values are given in Table 2.

A surface luminosity projected profile, in $\text{erg s}^{-1} \text{ kpc}^{-2}$, is obtained from the weighted (using w_i) histogram of projected separations to the galaxies (R_p) divided by the area in kpc^2 covered by each histogram bin: $\pi(R_1^1 - R_0^2)A_{\text{corr}}$. Conversely, an X-ray spectrum, in $\text{erg s}^{-1} \text{ keV}^{-1}$ in a given projected radial aperture is obtained with the weighted sum of the energies (E_{rf}) of all events in a given energy bin, divided by the width of that bin (in keV).

3.4. Background estimation and its uncertainties

The projected radial profiles and integrated spectra obtained with the random cubes represent the null hypothesis of no signal, and are used to assess the robustness of any possible detection from the stacking samples. We repeat this measurement process at random positions twenty times (using different random points each time). From the outer shells of the radial background profiles (500 kpc to 3000 Mpc) of the 20 realizations, we estimate the mean background luminosity. It takes values around $1.1 \times 10^{37} \text{ erg s}^{-1} \text{ kpc}^{-2}$. For each galaxy sample the background value obtained is different, indeed the total area covered and the masked area both vary from sample to sample.

The uncertainty due to the source masking procedure, see Sect. 3.2, suggests that the total number of event is subject at most to a residual 2% systematic uncertainty. So, to be conservative, we add a 2% systematic uncertainty to the mean value of the background: $\sigma^{BG} = 0.02$ i.e. at all scales and energies.

The uncertainty on the galaxy stack count rates follow a Poisson distribution: $\sigma^{GAL} = 1/\sqrt{N^{GAL}}$. The uncertainty on the final, background subtracted, measurement (i.e. galaxy minus background) is the quadratic sum of the two uncertainties: $\sqrt{(\sigma^{GAL})^2 + (\sigma^{BG})^2} = \sqrt{1/N^{GAL} + 0.02^2}$.

Additional sources of uncertainties may arise from the use of inaccurate redshifts, source positions or photon energies. Uncertainties on centering/positions could artificially cause the PSF to broaden; uncertainties on energies could cause spectral distortions; redshift uncertainties would cause both spectral and spatial distortions. Since we use spectroscopic redshifts, we consider the uncertainty coming from those to be negligible; however, one could imagine that a few catastrophically incorrect redshifts are included. If for example, these are additionally located in bright clusters (illustrative purpose), we would incorrectly convert arcminutes to kpc, which could cause either profiles to be more concentrated (redshift is lower than true redshift) or diluted (redshift measured is higher than true redshift). The exact quantification of a possible systematic arising from catastrophic redshift, incorrect source positions or photon energies is left for future studies.

3.5. Empirical point source profile and validation against AGN

As we are interested in detecting extended CGM X-ray emission around galaxies, a key prerequisite is an accurate characterization of the eROSITA Point Spread Function (PSF) and its convolution with the galaxies’ redshift distribution.

To obtain an empirical point source profile to compare to each galaxy sample, we repeat the procedure described in Sect. 3.3 with sets of detected X-ray point sources in eFEDS

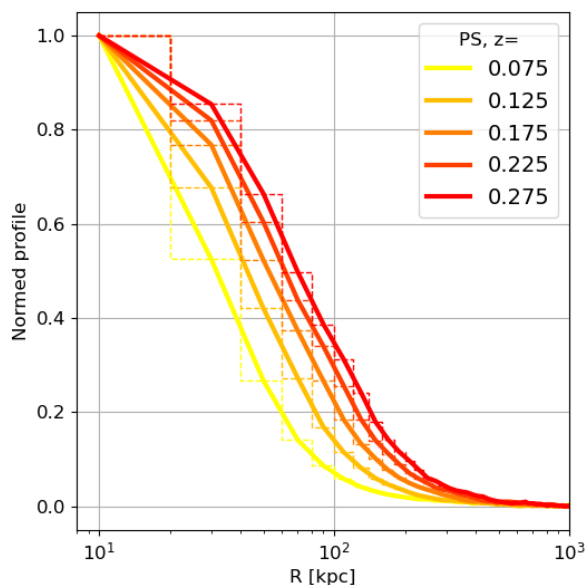


Fig. 3. eROSITA normalized point source profiles as a function of redshift in bins of 20kpc. Each curve represents the average point source profile in a redshift bin of width of 0.05: 0.05-0.1, 0.1-0.15, 0.15-0.2, 0.2-0.25, 0.25-0.3. The labelled number gives the mean redshift of the bin. At the mean redshift of the sample ($z \sim 0.2$), the half-width-half-maximum of the empirical PSF corresponds to about 60 kpc.

(‘point source cube’). We replace the galaxy positions (on sky) with positions of extra galactic point sources with moderately bright fluxes $10^{-14} < F_{0.2-2.3\text{keV}}/[\text{erg cm}^{-2} \text{s}^{-1}] < 10^{-12}$ and $\text{ERO_DET_LIKE} > 20$, taken from the Brunner et al. (2021) catalogue. All other galaxy quantities are kept, in particular the redshift.

In doing so, we convolve the eROSITA PSF with the redshift distribution of the galaxy sample, and we obtain the shape of the radial profile expected if all sources were bright and point-like in the eROSITA images. Figure 3 shows how these empirical PSF profiles (in kpc) evolve as a function of redshift. The higher the redshift, the broader the point source profile is. We do not stack beyond redshift 0.3 to avoid a too wide PSF in kpc. At the mean redshift of the sample ($z \sim 0.2$), the half-width-half-maximum of the empirical PSF corresponds to about 60 kpc.

We stress here that the purpose of this exercise is not to determine an accurate PSF profile for eROSITA (see e.g. Churazov et al. 2020), but rather to have a term of reference to assess the possible extended nature of the profiles measured around galaxies. Obviously, the stacked profiles obtained here from the detected point sources are by construction much brighter than the stacked galaxy profiles (see Sect. 4 below). To ease comparison, in each of the galaxy stack we present below, we re-scale the convolved PSF profile to match the central value of the galaxy profile, creating a ‘maximal Point Source’ (max PS) term of comparison³.

³ PSF profiles could be artificially broadened due to the clustering of the galaxies (Popesso et al. 2012). Complete simulations of the galaxy population and its X-ray emission would be needed over cosmological volumes to enable a quantitative assessment. Indeed, we need to generate a model to populate the full sky with X-ray emitting galaxies together with their circum galactic medium (possibly following simulations of the gas around galaxy clusters from Comparat et al. 2020a), which is beyond the scope of this article. We defer to future studies the quantification of this effect.

3.6. Validation

To validate the stacking procedure, we apply it to known (eFEDS-detected) active galactic nuclei (with measured spectroscopic redshift). We stack at the spectroscopic AGN redshift. Its integrated luminosity (in erg s^{-1}) amounts to $\log_{10}(L_X) = 42.72 \pm 0.08$, while the mean luminosity of the same AGN set as determined by Liu T et al. (2021) is $\log_{10}(L_X) = 42.75$. The background subtracted X-ray spectrum obtained is well fit by a power-law with a photon index of 2.05 ± 0.05 , compatible with the mean slope of 2.02 determined on the same sample by Liu T et al. (2021). So the projected luminosity profile and stacked spectra are in very good agreement with the mean of the measurements made on individual AGN.

4. Results

We discuss first the detection in the stacking experiment for the full sample (Sect. 4.1). We consider to have a ‘detection’ when the signal to noise is larger than 3, a ‘hint of detection’ if the signal to noise is between 1 and 3, and an ‘upper limit’ when the signal to noise is smaller than 1.

In Sections 4.2 and 4.3, we discuss the trends obtained when splitting the sample according to its specific star formation rate and stellar mass. The comparison with theoretical predictions presented in Sect. 5 is done on the binned samples, where the stellar population is best controlled.

4.1. Detection in the complete stack

We first report the results of our stacking exercise applied to the sample of 16,142 galaxies at a mean redshift 0.22 and a mean stellar mass of 10.7 (named ALL_M10.7). We focus here on the results obtained by three possible masking procedures: ‘ALL’, ‘M1’ and ‘M3’ (see definitions in Sect. 3.2).

When applying the ‘ALL’ mask we obtain a detection above the background, see Fig. 4, top left panel. The signal to noise is ~ 3 within $R_p < 80$ kpc. At larger radii (> 80 kpc), the signal measured (magenta crosses) is consistent with the background (green dashes). The shape of the profile is marginally more extended than the maximal point source profile (grey step line).

The detection significance increases when using the ‘M1’ mask (Fig. 4, top middle panel) i.e. when the galaxy clusters and groups detected by eROSITA in the GAMA galaxies’ redshift range are not removed before stacking. The signal to noise accumulated within $R < 80$ kpc is about ~ 5 (reported in Table 3). Compared to the ‘ALL’ mask profile, the ‘M1’ is brighter and significantly deviates from the maximal point source profile.

When using the ‘M3’ mask, i.e. when the galaxy clusters, groups and point sources detected by eROSITA among GAMA galaxies are not masked, the signal to noise within 80 kpc increases to ~ 13 , see Fig. 4 (top right panel), and Table 4. The overall stacked profile corresponds, qualitatively, to what is expected with the addition of one (or multiple) bright unresolved sources.

Finally, to measure the mean projected emission coming from around the galaxies, we subtract the background from each stacked profile, see Fig. 4, bottom panels. There, background-subtracted profiles are shown out to 300 kpc. The possible deviation from a point source emission profile is made clearer by the comparison with the corresponding ‘max PS’ profile. Using the background-subtracted profiles, we measure the integrated

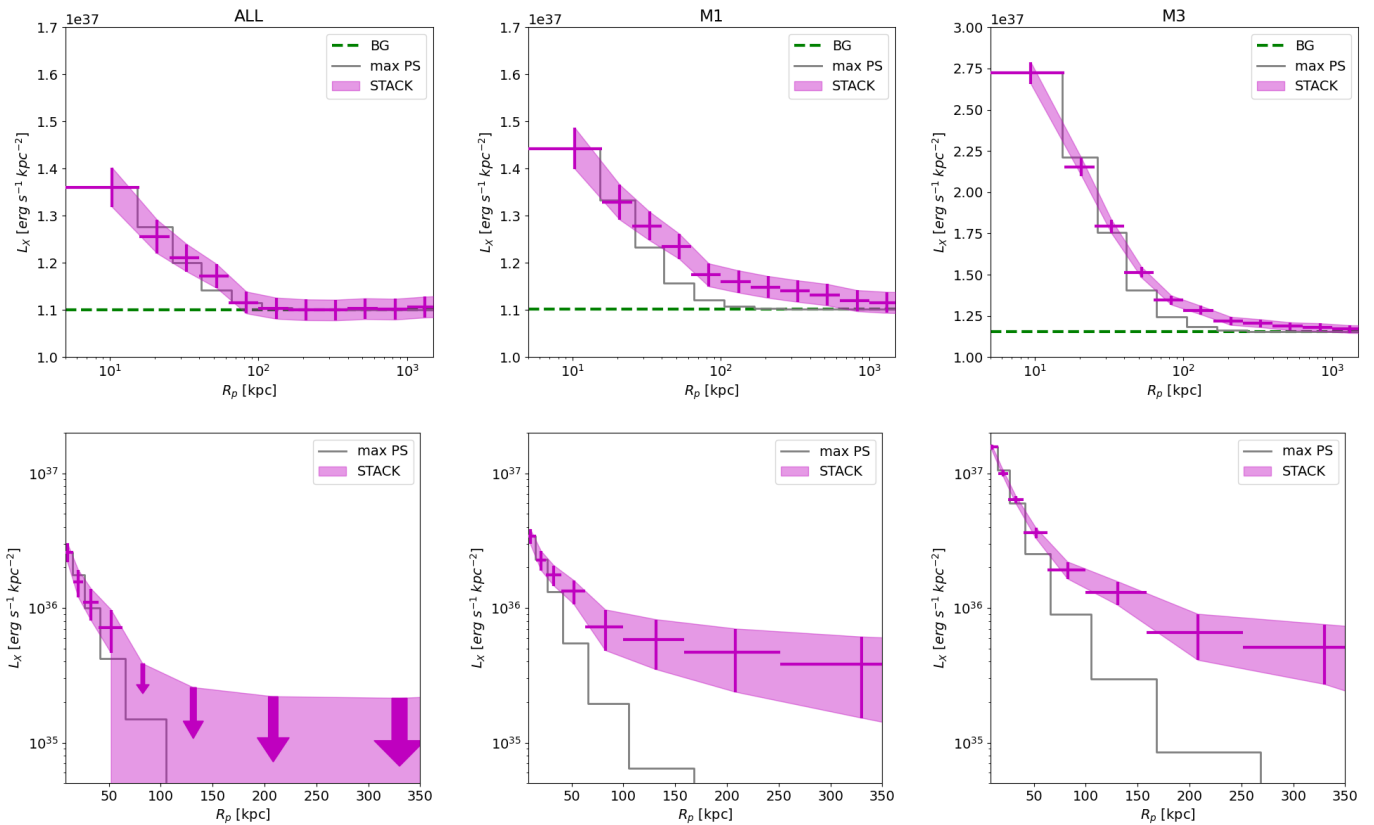


Fig. 4. Measured X-ray radial projected luminosity profiles (0.5–2.0 keV rest-frame) for the ALL_M10.7 GAMA central galaxy sample (‘STACK’, magenta crosses and shaded area). Each panel shows the result when a different mask is applied to the set of events: ‘ALL’ (left), ‘M1’ (middle), ‘M3’ (right). Note the variation in the y-axis range in different panels. The green dashed line represents the background level, estimated as discussed in Sect. 3.4. The profile shape expected if all sources stacked were point-like is shown with a grey line labeled ‘max PS’. The bottom series of panels shows the background-subtracted profiles with a linear radial scale extending to 300 kpc.

projected luminosity in an aperture R_p (in kpc) as follows:

$$L_X^{<R_p} = \int_{r=0}^{r=R_p} [L_X(r) - BG] 2\pi r dr, \quad (5)$$

where BG is the background level estimated as in Sect. 3.4. For each sample, the measured luminosity is reported for two apertures: 80 and 300 kpc, in the Tables 3 (for mask M1) and 4 (for mask M3).

The expected total (or radially-integrated) XRB luminosity for the ALL_M10.7 sample is 1.1×10^{40} erg s $^{-1}$. For the M1 (M3) mask, the luminosity measured in the inner 80 kpc is $2.8 \pm 0.5 \times 10^{40}$ ($8.8 \pm 0.7 \times 10^{40}$) erg s $^{-1}$; therefore, the observed luminosity cannot solely come from XRB.

The complete stack being constituted of a varied mix of different galaxies, linking the detection to underlying physical processes is complex. To further interpret the link between the detected emission and its possible sources (hot gas, XRB, faint AGN) we split the GAMA sample according to physical properties of the galaxies, as we describe in the following sections.

4.2. Trend with specific star formation rate at fixed stellar mass $\sim 5 \times 10^{10} M_\odot$

We split the sample into a quiescent sub-sample and a star-forming sub-sample. We set a maximum boundary in stellar mass at $10^{11} M_\odot$, which corresponds to haloes with a mass of $\sim 5 \times 10^{12} M_\odot$ (using the stellar to halo mass relation from Moster

et al. 2013), well below the halo mass of groups and clusters. We then search for the lower stellar mass boundary so that both samples have a mean mass of $\log_{10}(M^*/M_\odot) \sim 10.7$, around the turn over (knee) of the stellar mass function, often called M^* (Ilbert et al. 2013). We name these samples QU_M10.7 for the quiescent galaxies and SF_M10.7 for the star-forming galaxies. The mean redshift of each sample is close: 0.2 for QU_M10.7 and 0.23 for SF_M10.7, a 0.3 Gyr difference. The sSFR of QU_M10.7 is more than 100 times smaller than that of SF_M10.7. Their redshift and stellar mass distributions are shown in Fig. 5; the SF sample is biased towards higher redshift and lower mass galaxies compared to the QU sample.

The galaxies in these samples typically live in dark matter haloes of $5 - 50 \times 10^{11} M_\odot$ with a mean at $\sim 1.6 \times 10^{12} M_\odot$, where the conversion of baryons into stars is thought to be the most efficient (Behroozi et al. 2013; Moster et al. 2013). At this stellar mass, Velander et al. (2014) found that the red galaxies reside in denser environments than blue galaxies. They measured the host halo mass of blue and red $\sim M^*$ galaxies, and found that it was comprised between $1-3 \times 10^{12} M_\odot$ for both. Based on these results, we conclude that the samples QU_M10.7 and SF_10.7 are hosted on average by similarly massive haloes, and, importantly, live in different environments.

With the M1 mask

In both cases, there is an X-ray detection in the stacks obtained with the M1 mask, see Fig. 6. For the QU_M10.7 (SF_M10.7)

Table 3. Cylindrical projected X-ray luminosity using the M1 mask.

sample name	$\log_{10}(M_{vir})$ halo	S/N		L_X [10^{40} erg s^{-1}]			
		80	300	XRB	max PS	$R_p < 80$ kpc	$R_p < 300$ kpc
ALL_M10.7	12.2	5.2	2.3	$1.1^{+0.3}_{-0.2}$	2.8	2.8 ± 0.5	15.4 ± 6.6
Fixed stellar mass selection							
QU_M10.7	12.2	7.3	4.3	$0.6^{+0.2}_{-0.1}$	3.1	4.0 ± 0.5	28.7 ± 6.6
SF_M10.7	12.2	3.6	0.9	$1.4^{+0.4}_{-0.3}$	2.6	1.9 ± 0.5	5.7 ± 6.7
Quiescent galaxies							
QU_M11.71	15.0	10.9	10.3	$7.1^{+2.1}_{-1.6}$	92.2	82.2 ± 7.6	440.7 ± 42.6
QU_M11.58	14.5	8.5	7.5	$5.3^{+1.6}_{-1.2}$	78.0	70.0 ± 8.2	314.3 ± 42.1
QU_M11.54	14.4	3.9	5.0	$4.8^{+1.4}_{-1.1}$	24.8	22.3 ± 5.7	174.1 ± 35.0
QU_M11.35	13.8	8.6	7.0	$3.0^{+0.9}_{-0.7}$	17.1	14.9 ± 1.7	87.5 ± 12.5
QU_M11.2	13.2	8.4	4.4	$2.1^{+0.6}_{-0.5}$	10.0	8.9 ± 1.1	40.5 ± 9.2
QU_M11.04	12.8	6.3	4.5	$1.5^{+0.4}_{-0.3}$	3.7	5.0 ± 0.8	36.7 ± 8.2
QU_M10.88	12.5	6.1	5.2	$1.0^{+0.3}_{-0.2}$	3.8	4.6 ± 0.8	41.5 ± 8.0
QU_M10.73	12.3	5.7	3.1	$0.7^{+0.2}_{-0.1}$	2.9	3.9 ± 0.7	22.4 ± 7.2
QU_M10.53	12.0	5.5	3.5	$0.4^{+0.1}_{-0.1}$	2.4	3.2 ± 0.6	22.5 ± 6.4
star-forming galaxies							
SF_M11.25	13.4	3.3	1.7	$4.0^{+1.3}_{-1.0}$	10.3	5.7 ± 1.7	21.8 ± 12.7
SF_M11.12	13.0	2.5	1.5	$3.1^{+1.0}_{-0.7}$	7.9	4.1 ± 1.6	18.8 ± 12.2
SF_M11.05	12.8	2.4	1.7	$2.6^{+0.8}_{-0.6}$	4.8	3.7 ± 1.6	20.6 ± 11.9
SF_M10.99	12.7	3.5	1.3	$2.4^{+0.7}_{-0.6}$	5.3	3.7 ± 1.0	12.1 ± 9.1
SF_M10.9	12.5	3.2	1.2	$2.0^{+0.6}_{-0.5}$	3.3	3.1 ± 1.0	10.1 ± 8.7
SF_M10.86	12.4	3.0	1.1	$1.9^{+0.6}_{-0.5}$	3.5	2.3 ± 0.8	8.5 ± 7.7
SF_M10.74	12.3	2.8	0.6	$1.6^{+0.5}_{-0.4}$	3.3	2.1 ± 0.7	4.3 ± 7.5
SF_M10.63	12.1	2.8	0.7	$1.3^{+0.4}_{-0.3}$	3.1	2.0 ± 0.7	5.3 ± 7.3
SF_M10.52	12.0	1.8	0.6	$1.2^{+0.3}_{-0.3}$	0.8	1.2 ± 0.7	4.2 ± 7.0
SF_M10.41	11.9	2.5	0.8	$1.0^{+0.3}_{-0.2}$	1.5	1.6 ± 0.7	5.8 ± 6.9
SF_M10.3	11.8	1.9	0.5	$0.9^{+0.2}_{-0.2}$	1.8	1.2 ± 0.6	3.4 ± 6.5
SF_M10.18	11.8	2.9	-0.0	$0.7^{+0.2}_{-0.1}$	1.3	1.7 ± 0.6	-0.2 ± 6.2
SF_M10.03	11.6	2.1	0.5	$0.6^{+0.2}_{-0.1}$	1.4	1.1 ± 0.5	2.8 ± 5.9
SF_M9.86	11.5	-0.2	-0.4	$0.4^{+0.1}_{-0.1}$	0.3	-0.1 ± 0.4	-2.3 ± 5.3
SF_M9.64	11.4	1.3	0.3	$0.3^{+0.1}_{-0.1}$	0.3	0.5 ± 0.4	1.5 ± 4.8

Notes. Cylindrical projected luminosity, in units of 10^{40} erg s^{-1} , measured within projected distance of 80 and 300 kpc for each sample with the M1 mask. In the column S/N is reported the signal to noise of the measurement. We consider to have a ‘detection’ when the signal to noise is larger than 3, a ‘hint of detection’ if the signal to noise is between 1 and 3, and an ‘upper limit’ when the signal to noise is smaller than 1. They are compared with the XRB model prediction of [Aird et al. \(2017\)](#). ‘max PS’ is the luminosity obtained when integrating the point source profiles (grey lines in the figures), which constitutes an upper limit to the luminosity that can be attributed to point source emission. $\log_{10}(M_{vir})$ is the estimated mean halo mass obtained using the stellar to halo mass relation from [Moster et al. \(2013\)](#). Table 4 reports the same quantities as obtained when applying the ‘M3’ mask.

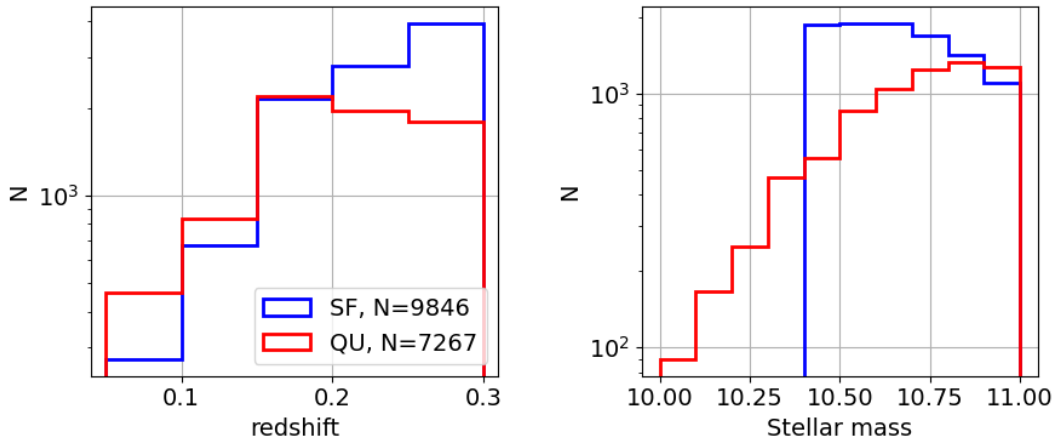


Fig. 5. Redshift and stellar mass distributions of the two QU_M10.7 and SF_M10.7 samples. Although the samples share a similar mean stellar mass (10.66 and 10.72) and a similar mean redshift (0.2 and 0.23), the underlying distributions differ.

Table 4. Cylindrical projected X-ray luminosity as in Table 3, but using the M3 mask.

sample name	$\log_{10}(M_{vir})$ halo	S/N		$L_X [10^{40} \text{ erg s}^{-1}]$			
		80	300	XRB	max PS	$R_p < 80 \text{ kpc}$	$R_p < 300 \text{ kpc}$
ALL_M10.7	12.2	13.1	4.0	1.1 ^{+0.3} _{-0.2}	11.3	8.8 ± 0.7	29.2 ± 7.2
Fixed stellar mass selection							
QU_M10.7	12.2	8.3	4.6	0.6 ^{+0.2} _{-0.1}	4.1	4.9 ± 0.6	31.8 ± 6.9
SF_M10.7	12.2	14.9	3.5	1.4 ^{+0.4} _{-0.3}	16.0	11.2 ± 0.7	25.5 ± 7.4
Quiescent galaxies							
QU_M11.71	15.0	11.8	10.4	7.1 ^{+2.1} _{-1.6}	111.4	97.4 ± 8.3	459.0 ± 44.0
QU_M11.58	14.5	9.2	7.6	5.3 ^{+1.6} _{-1.2}	83.9	74.2 ± 8.1	319.2 ± 42.0
QU_M11.54	14.4	6.3	5.5	4.8 ^{+1.4} _{-1.1}	57.9	42.3 ± 6.7	199.5 ± 36.6
QU_M11.35	13.8	11.0	7.0	3.0 ^{+0.9} _{-0.7}	25.0	19.5 ± 1.8	89.8 ± 12.8
QU_M11.2	13.2	8.9	4.6	2.1 ^{+0.6} _{-0.5}	11.4	9.9 ± 1.1	44.6 ± 9.7
QU_M11.04	12.8	8.3	4.7	1.5 ^{+0.4} _{-0.3}	5.5	7.0 ± 0.8	40.3 ± 8.6
QU_M10.88	12.5	7.1	5.6	1.0 ^{+0.3} _{-0.2}	5.1	5.8 ± 0.8	47.2 ± 8.5
QU_M10.73	12.3	6.6	3.3	0.7 ^{+0.2} _{-0.1}	4.2	4.8 ± 0.7	25.0 ± 7.5
QU_M10.53	12.0	5.5	3.6	0.4 ^{+0.1} _{-0.1}	2.5	3.3 ± 0.6	23.7 ± 6.7
star-forming galaxies							
SF_M11.25	13.4	15.8	5.5	4.0 ^{+1.3} _{-1.0}	62.8	38.4 ± 2.4	78.0 ± 14.2
SF_M11.12	13.0	13.9	5.3	3.1 ^{+1.0} _{-0.7}	55.2	30.6 ± 2.2	73.5 ± 13.8
SF_M11.05	12.8	8.4	3.9	2.6 ^{+0.8} _{-0.6}	26.5	16.8 ± 2.0	51.1 ± 13.0
SF_M10.99	12.7	11.4	3.3	2.4 ^{+0.7} _{-0.6}	24.6	15.6 ± 1.4	33.4 ± 10.0
SF_M10.9	12.5	12.5	5.3	2.0 ^{+0.6} _{-0.5}	18.3	16.0 ± 1.3	52.3 ± 9.9
SF_M10.86	12.4	15.3	4.8	1.9 ^{+0.6} _{-0.5}	21.8	15.1 ± 1.0	41.6 ± 8.6
SF_M10.74	12.3	14.7	3.2	1.6 ^{+0.5} _{-0.4}	21.7	15.4 ± 1.0	26.0 ± 8.2
SF_M10.63	12.1	10.2	2.0	1.3 ^{+0.4} _{-0.3}	14.4	8.9 ± 0.9	15.3 ± 7.8
SF_M10.52	12.0	10.6	3.8	1.2 ^{+0.3} _{-0.3}	10.5	9.1 ± 0.9	30.2 ± 7.9
SF_M10.41	11.9	8.0	1.8	1.0 ^{+0.3} _{-0.2}	7.9	6.2 ± 0.8	13.3 ± 7.4
SF_M10.3	11.8	4.9	0.7	0.9 ^{+0.2} _{-0.2}	5.1	3.3 ± 0.7	4.8 ± 6.8
SF_M10.18	11.8	9.1	1.4	0.7 ^{+0.2} _{-0.1}	4.8	6.4 ± 0.7	9.5 ± 6.6
SF_M10.03	11.6	4.3	1.5	0.6 ^{+0.2} _{-0.1}	3.2	2.5 ± 0.6	9.5 ± 6.3
SF_M9.86	11.5	1.5	1.6	0.4 ^{+0.1} _{-0.1}	1.1	0.7 ± 0.5	9.4 ± 5.8
SF_M9.64	11.4	1.8	1.1	0.3 ^{+0.1} _{-0.1}	0.4	0.7 ± 0.4	5.7 ± 5.1

sample, the cumulative signal to noise ratio within 80 and 300 kpc is of 7.3 (3.6) and 4.3 (0.9). In the case of the QU_M10.7 sample, the emission is clearly extended and not centrally peaked, see Fig. 6, left panels. For the SF_M10.7 sample, the emission is centrally peaked and consistent with a maximal PSF profile, see Fig. 6, right panels. With a direct comparison of the background subtracted profiles in Fig. 7 (left panel) the difference between QU_M10.7 and SF_M10.7 is made obvious. At scales larger than 100 kpc, the quiescent galaxy profile is at least two times brighter than that of the star-forming galaxies.

Our measurement, using a nearly complete galaxy catalogue, sets a firm observational evidence: at the same mean stellar mass of $\sim 5 \times 10^{10} M_{\odot}$, star-forming galaxies show significantly less projected X-ray emission on large scales in the 0.5–2 keV rest-frame energy range. The possibility of such a difference between passive and star-forming $\sim M^*$ galaxies was previously suggested by Bregman et al. (2018), hinting at a difference in their evolutionary histories.

The shallow slope measured in the QU profile might come from projection effects (see discussion in Sect. 6.2) due to the fact that, as mentioned before, quiescent galaxies tend to live in denser, hotter environments (e.g. Velander et al. 2014).

With the M3 mask

Figure 8 shows the projected luminosity profiles obtained with the M3 mask. When including the detected X-ray point sources, the central parts of the profiles increases significantly for the SF profile, mainly due to the contribution of bright AGN (see Sect. 3.2.1), while for the QU profile the increase is less noticeable. Differently to the M1 stack, there is a hint of extended emission in the SF background subtracted profile. The right panel of Fig. 7 compares the background subtracted projected profiles with the M3 mask applied.

Projected luminosity within 80 and 300 kpc

The integrated projected luminosity (within 80 and 300 kpc apertures) is reported in Tables 3 (M1) and 4 (M3).

With the M1 mask, for QU_M10.7 the emission within 80 kpc is $L_X = 4.0 \pm 0.5 \times 10^{40} \text{ erg s}^{-1}$, almost an order of magnitude larger than the corresponding prediction for the unresolved XRB luminosity from Aird et al. (2017) $L_X = 6 \times 10^{39} \text{ erg s}^{-1}$. Given this, and the fact that the QU_M10.7 galaxies profile is clearly extended, we may conclude that this emission is mainly coming from both the hot gas in the CGM of the individual galaxies and from the projection of the large scale environment around them. Differently, the SF_M10.7 emission within 80 kpc amounts to $1.9 \pm 0.5 \times 10^{40} \text{ erg s}^{-1}$, which is compatible

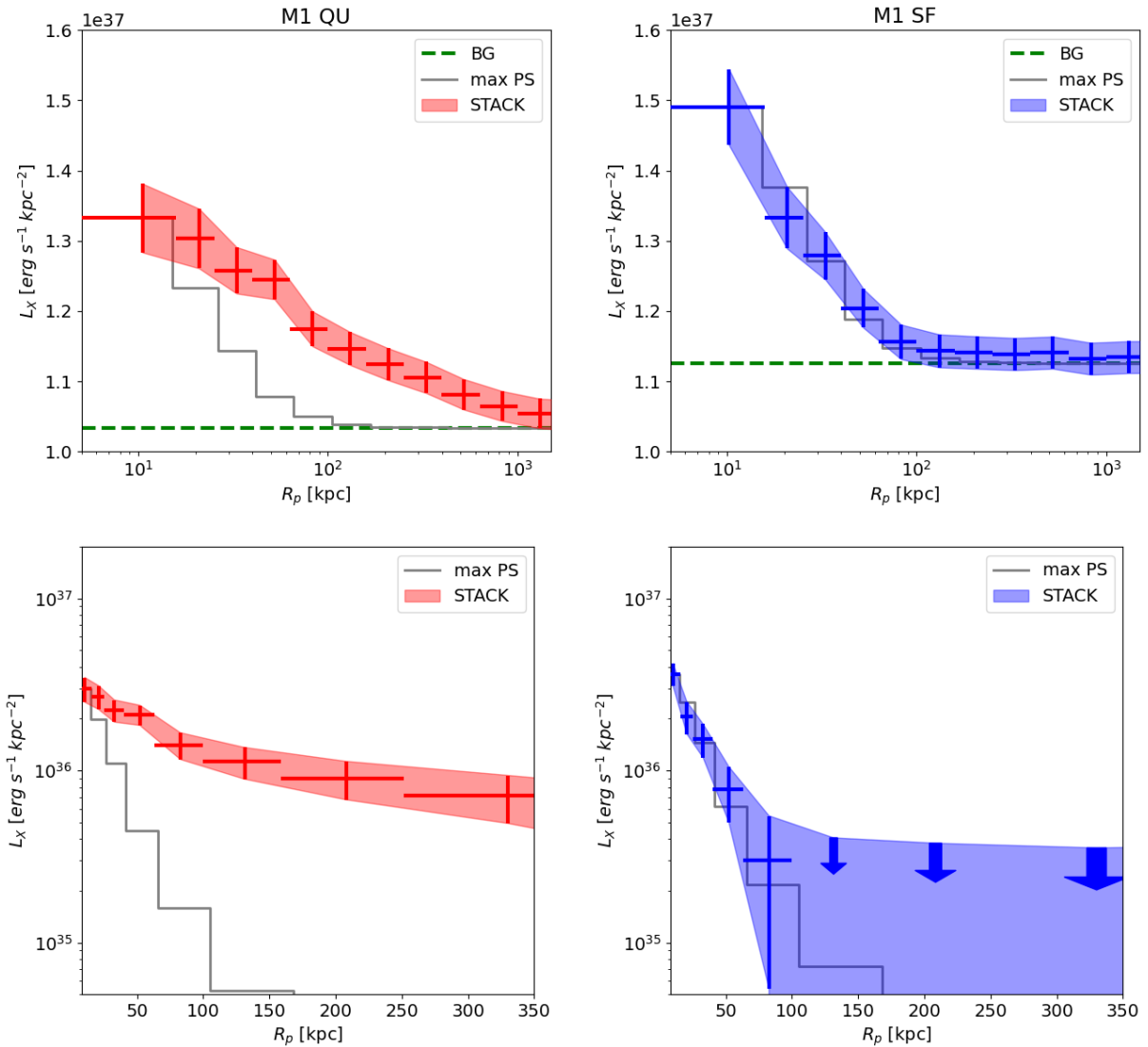


Fig. 6. Measured X-ray radial projected luminosity profiles (0.5–2.0 keV rest-frame) for the quiescent QU_M10.7 (left, red) and star-forming SF_M10.7 (right, blue) samples of central galaxies, using the M1 mask. Both samples have the same mean stellar mass of $\sim 10^{10.7} M_{\odot}$ and mean redshift of $z \sim 0.2$ (but see the underlying distributions in Fig. 5). QU_M10.7 (left) shows a clearly extended profile, while SF_M10.7 (right) has a profile compatible with that of a point source convolved with the eROSITA PSF (grey). The bottom row shows the corresponding background-subtracted profiles.

within 1σ with that expected from X-ray binaries ($1.4^{+0.4}_{-0.3} \times 10^{40}$ erg s^{-1}). The profile also does not appear extended. We are led to conclude that around star-forming galaxies of a mean mass of $\log_{10}(M^*/M_{\odot}) \sim 10.7$, an extended hot gas component is not significantly detected. We refer the reader to Sect. 6.1 for a more comprehensive discussion of the AGN contamination.

With the M3 mask, compared to the M1 mask, the luminosity of the QU sample increases by 20% while for the SF, it increases by almost a factor of 6. There may be a hint of extent emission in the SF profile measured on the larger scales between 200 and 300 kpc.

4.3. Trends with stellar mass

We further investigate trends as a function of stellar mass and specific star formation rate with the set of samples specified in Table 1. For the quiescent samples, we are limited by the total number of galaxies available in the catalogue and unfortunately

we are not able to create lower mass bins. For the star-forming samples, we define samples down to stellar masses of $3 \times 10^9 M_{\odot}$. For the M1 mask, we report a detection ($S/N > 3$ in 80 or 300 kpc) for all quiescent samples and only for a handful of the star-forming galaxy samples, see Table 3. For the M3 mask, we report a detection for all samples except for the star-forming samples with a stellar mass lower than $10^{10} M_{\odot}$, see Table 4.

The set of background subtracted projected luminosity profiles obtained in the M1 (M3) mask are shown in Fig. 9, left (right) panels. The qualitative trend observed for the quiescent samples (M1 or M3 mask) is in line with expectations: the higher the stellar mass (and thus host halo mass), the brighter the emission and the higher the signal to noise (Tables 3, 4). For the star-forming samples, with the M1 mask, all profiles, but those at the highest-mass end, are broadly consistent with one another on large scales and are dominated by noise. A difference between profiles arises in the first radial bins, e.g. the mean brightness of the central point source scales with the stellar mass. For the

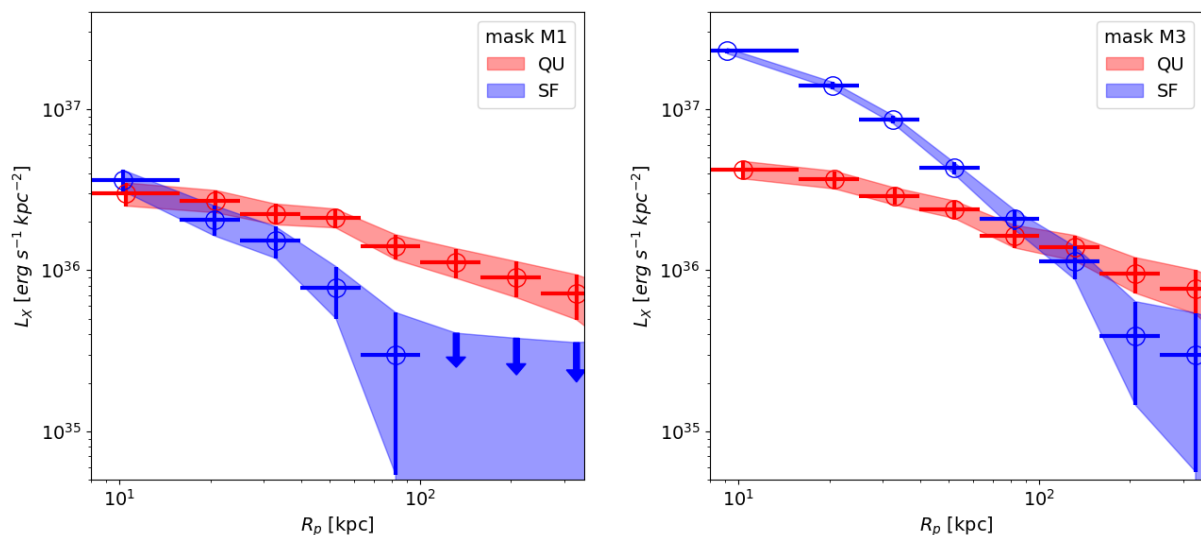


Fig. 7. Comparison of the background-subtracted projected luminosity profiles (0.5–2.0 keV rest-frame) of the star-forming sample SF_M10.7 and the quiescent sample QU_M10.7, i.e. of star-forming vs. quiescent galaxies at similar median stellar mass around the scale of the Milky Way and Andromeda, albeit in the range $0.05 < z < 0.3$. In the left (right) panel, results are given for the M1 (M3) mask and are the same as those of Fig. 6 (8).

star-forming samples with the M3 mask, the amplitude correlates with stellar mass at all scales, like for the QU profiles. This follows the expectation that the mean AGN luminosity is correlated with the host stellar mass (Aird et al. 2017; Comparat et al. 2019; Georgakakis et al. 2019). Possible extended emission around star-forming galaxies remains to be significantly detected.

4.4. Scaling between X-ray projected luminosity and stellar mass, M1 mask

Figure 10 shows the scaling measured between X-ray luminosity and stellar mass within 300 kpc (main panel), in the inner 80 kpc (bottom left) and in the shell 80–300 kpc (bottom right), all obtained with the M1 mask applied. Overall the signal to noise is highest in the central 80kpc, see Table 3. It decreases when integrating to 300kpc. Indeed extending the integration to larger scales, the signal increases marginally while the noise increases much more, resulting in lower signal to noise. We find that the X-ray luminosity correlates with the mean stellar mass. The trend for star-forming galaxies is different from that of quiescent galaxies. However, there appear to be two regimes in the scaling between X-ray projected luminosity and stellar mass. The inner parts’ emission is dominated by point sources (AGN and XRB). The outer parts’ emission is dominated by CGM emission.

In particular, within 80 kpc, the slope of both SF and QU galaxies is similar to (but offset from) that predicted for XRB, and consistent with the predicted unresolved AGN population (orange shaded area, Comparat et al. 2019). The AGN population is predicted using eROSITA mock catalogues filtered on X-ray flux and optical magnitude to keep un-detected X-ray AGN that are optically brighter than the magnitude limit of GAMA: $F_X < 6.5 \times 10^{-15} \text{ erg cm}^{-2} \text{ s}^{-1}$ and $r < 19.8$. Those simulated AGN could be hosted by GAMA galaxies but would not have been detected in eFEDS. The simulations used start to be incomplete at stellar masses of $10^{10} M_\odot$ at $z = 0.22$, we thus limit the prediction to above this mass.

Still within 80 kpc (bottom left panel), only for the highest stellar mass quiescent galaxy samples, i.e. for stellar mass $> 2 \times 10^{11}$, corresponding to a halo mass $\geq 5 \times 10^{13}$, we measure a luminosity that is significantly brighter than the predicted point source emission. This is due to the large amount of hot gas in projection present in galaxy groups and galaxy clusters.

Within 300 kpc, the X-ray luminosity measured around SF samples is consistent with the predicted average point sources’ emission (combination of AGN plus XRB, dominated by AGN emission). For stellar masses above 10^{11} , the emission is marginally brighter than the expected point source contribution.

We look at the 80–300 kpc shell show on the bottom right hand panel of Fig. 10. For the quiescent sample and stellar masses above $\log M^* \sim 11.2$, the measurements are in good agreement with Anderson et al. (2015)⁴. Below $\log M^* \sim 11.2$, the luminosity measured is significantly above that of Anderson et al. (2015). We believe this is due to projection effects for the QU sample that preferentially lives in dense and hot environment. We discuss this effect in Sect. 6.2.

Still in the 80–300 kpc shell, for the star-forming samples, we only measure upper limits to the extended emission, except for the three highest stellar mass samples, where, however, the error bars extend to a low luminosity value, meaning only marginal detection, with signal to noise ~ 1.3 .

4.5. Scaling between X-ray projected luminosity and stellar mass, M3 mask

The relation obtained with the M3 mask is to be interpreted as the sum of all emitting entities: AGN, XRB, hot gas, augmented by systematic projection effects. In that regard, there is no need to split as a function of projected separation. Figure 11 shows the scaling measured in the inner 300 kpc with the M3 mask applied.

We predict the AGN, the galaxy group and the galaxy cluster population using the eROSITA mock catalogue methods (Com-

⁴ The slight discrepancy at the highest mass is likely due to the difference in aperture: 500c is larger than 300 kpc for a $10^{15} M_\odot$ halo

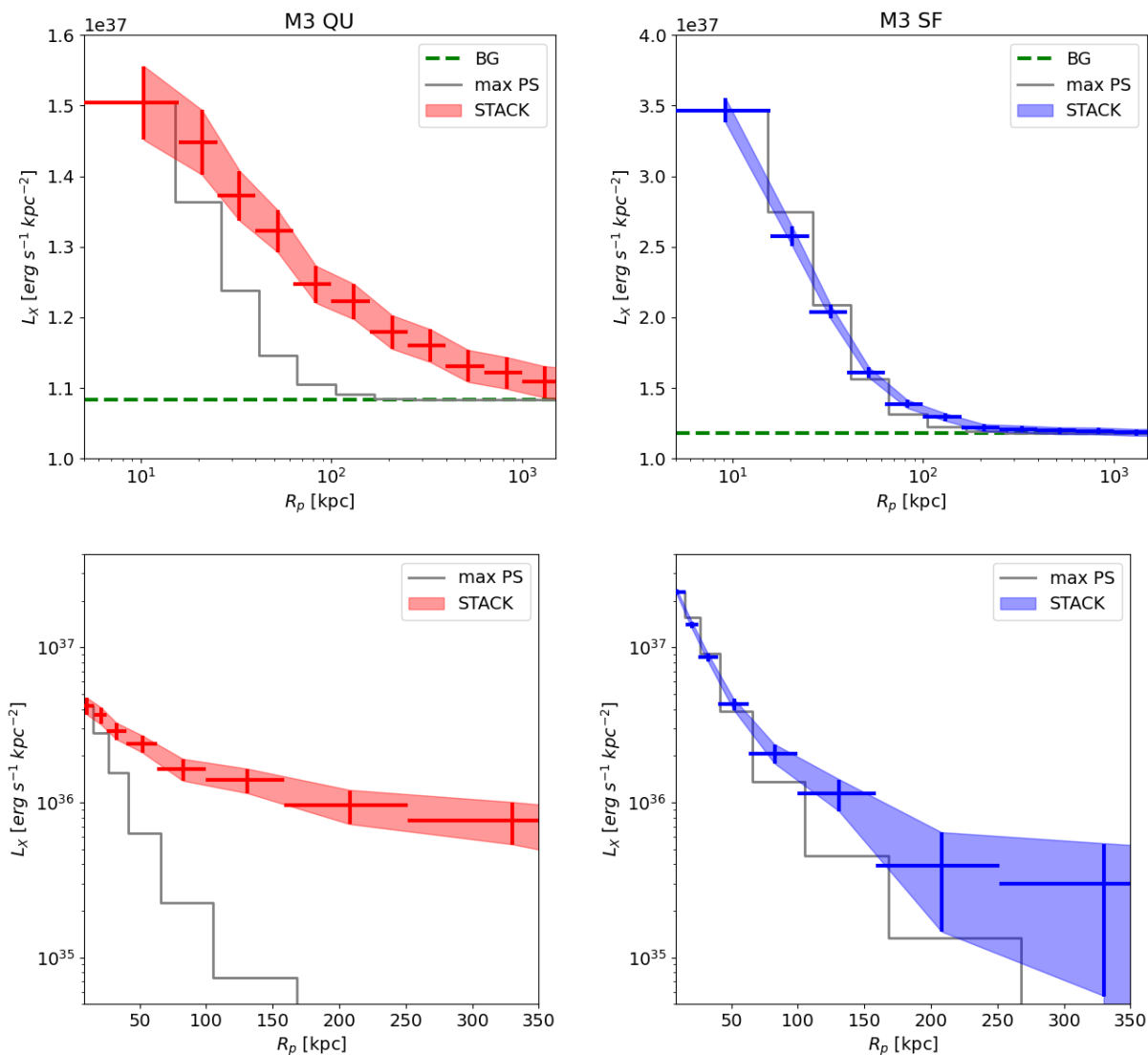


Fig. 8. Same as Fig. 6, with the M3 mask.

parat et al. 2019, 2020a, Seppi et al. in preparation). For the AGN population we select all X-ray AGN that are optically brighter than the magnitude limit of GAMA: $r < 19.8$. These model AGN could be hosted by GAMA galaxies regardless of the fact that they are (or not) detected in eFEDs. For the cluster and group population, no filter is applied. The black dashes represent the sum of the AGN and cluster contribution to this relation. We find that the luminosity – stellar mass relation is in good agreement with the models, which demonstrates that the Comparat et al. (2019, 2020a, Seppi et al. in preparation) are good models of the large scale structure seen in the X-ray.

At high mass, above $2 \times 10^{11} M_{\odot}$, the measurements are slightly below the model. This is likely due to the fixed 300 kpc aperture used, which for these masses is smaller than the R_{500c} used in the cluster model. For masses below $2 \times 10^{10} M_{\odot}$, measurements are consistent with the AGN model prediction, meaning that a detection of CGM emission is unlikely. For stellar masses between $2 \times 10^{10} M_{\odot}$ and $2 \times 10^{11} M_{\odot}$, the positive offset between the observations and models, is likely related to emission from the circum galactic medium and to projection effects. Given the uncertainties on the measurement and the large

scatter in the model prediction, it is complex to quantitatively assess the difference between the observation and the models.

5. Comparison with simulated galaxies

We elect the IllustrisTNG (hereafter TNG, Pillepich et al. 2018; Nelson et al. 2018; Naiman et al. 2018; Marinacci et al. 2018; Springel et al. 2018) and the EAGLE simulations (Schaye et al. 2015; Crain et al. 2015) as our reference points for the comparison of the results uncovered by eROSITA with the predictions from current, state-of-the-art cosmological hydrodynamical simulations of galaxies. The reasons are multi-fold. Firstly, both numerical projects provide flagship runs that encompass large enough volumes, and hence, large enough numbers of galaxies for the construction of samples comparable to the ones inspected in this paper — there are 6,478 and 3,557 galaxies with galaxy mass $\log_{10} M^* > 10$ in the TNG100 (TNG) and Ref-L0100N1504 (EAGLE) boxes, respectively, solely at $z = 0$. This would not be the case with zoom-in projects, which for massive galaxies are limited to examples of a few to a few tens. Secondly, their outcomes have been contrasted to an ever-increasing set of observables, with galaxy populations at low and

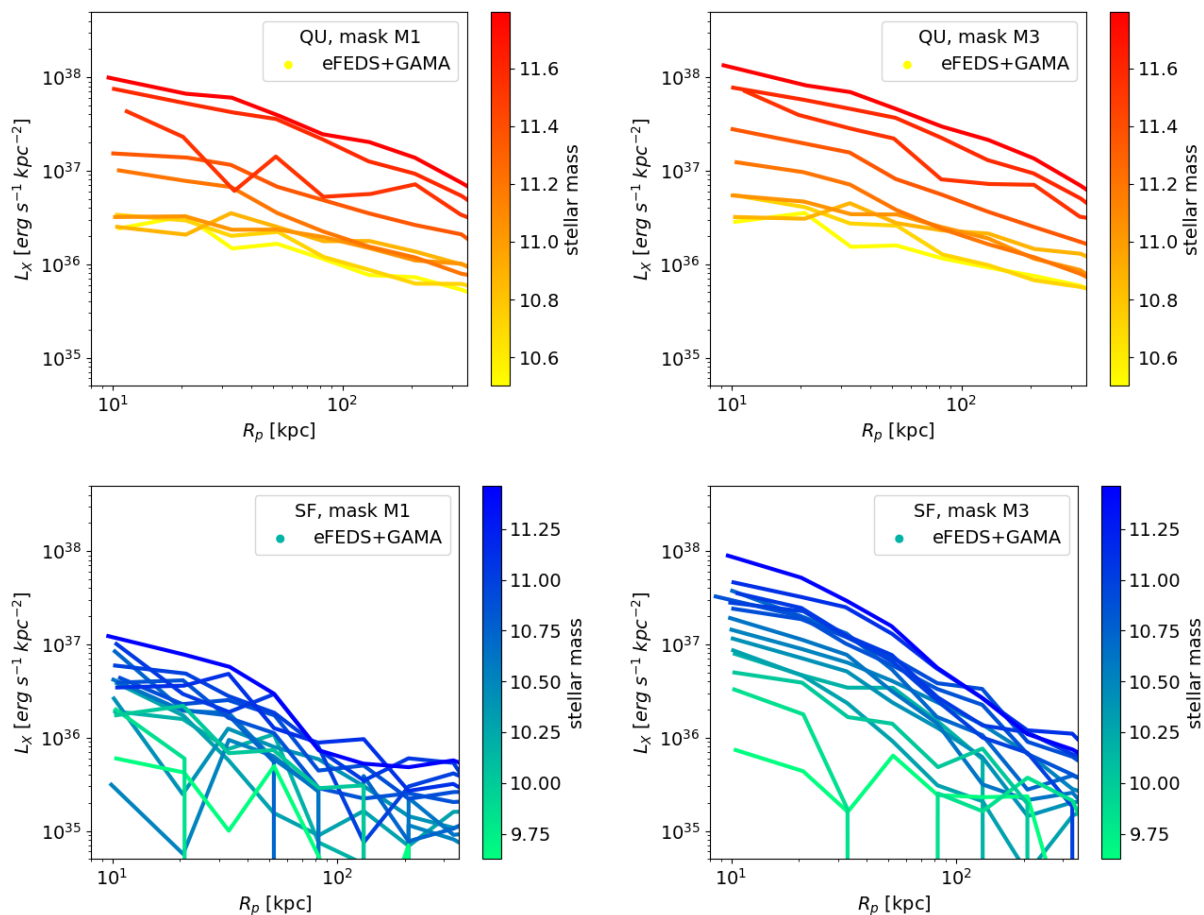


Fig. 9. Comparison of the background subtracted projected luminosity profiles in the 0.5–2.0 keV rest-frame band (M1 mask, left panels; M3 mask, right panels) for quiescent (top) and star-forming (bottom) samples as a function of galaxy stellar mass. star-forming profiles are compatible with point source emission while quiescent profiles are clearly extended.

intermediate redshift that are well in the ball park (< 1 dex) of observational constraints both in terms of demographics and inner galaxy properties. For example, the TNG simulations have been shown to well reproduce the low-redshift results obtained from Sloan Digital Sky Survey data in relation to: the $(g - r)$ color distributions across galaxy masses (Nelson et al. 2018); the quiescent fractions of both centrals and satellites as a function of stellar mass (Donnari et al. 2021); and the small and large-scale spatial clustering of galaxies, also when split by galaxy color (Springel et al. 2018). Thirdly, in both cases, predictions for the X-ray emission of the gas within and around galaxies at $z \sim 0$ have been already extensively quantified, across a wide range of masses, galactocentric distances, and for star-forming and quiescent galaxies separately (Truong et al. 2020; Oppenheimer et al. 2020). For example, in the 0.5–2 keV band, the $L_X(< R_{500c})$ vs. M_{500c} scaling relations of TNG are in the ball park of observational constraints by e.g. Pratt et al. (2009); Vikhlinin et al. (2009); Sun (2012); Mehtens et al. (2012); Lovisari et al. (2015) throughout the $10^{13-15} M_{\odot}$ range (Pop et al. in prep.). Similarly does EAGLE (Barnes et al. 2017). Finally, TNG and EAGLE are publicly available (Nelson et al. 2019; McAlpine et al. 2016).

5.1. Extraction of the CGM observables from the simulated data

Firstly, we construct simulated galaxy samples that are matched to the observed ones by finding, for each galaxy in the GAMA set, its simulated equivalent in TNG and EAGLE. The details of this procedure are given in Appendix A. In practice, results are shown by averaging across 20 Monte Carlo samples of TNG100 and EAGLE galaxies matched to the GAMA sample adopted in this paper.

Secondly, X-ray photons are not explicitly modeled by the TNG and EAGLE simulations. However, the X-ray intrinsic luminosity that would be emitted by the simulated galaxies can be derived given the physical properties of the gas (i.e. of the plasma) returned and predicted by the numerical model. In practice, here we rely on the mapping between observed eROSITA photon count rates and X-ray fluxes adopted throughout and described in Sect. 3. However, we only model the X-ray emission from the volume-filling gas, i.e. we do not attempt to model the contamination from XRB nor AGN.

For any gas cell or gas particle in the simulations, barring the star-forming ones and each characterized by a density, temperature and metallicity, we obtain the [0.5–2] keV luminosity assuming a single-temperature Astrophysical Plasma Emission Code, APEC 3.0.9, as implemented in the XSPEC⁵ (Smith et al.

⁵ <https://heasarc.gsfc.nasa.gov/xanadu/xspec/>

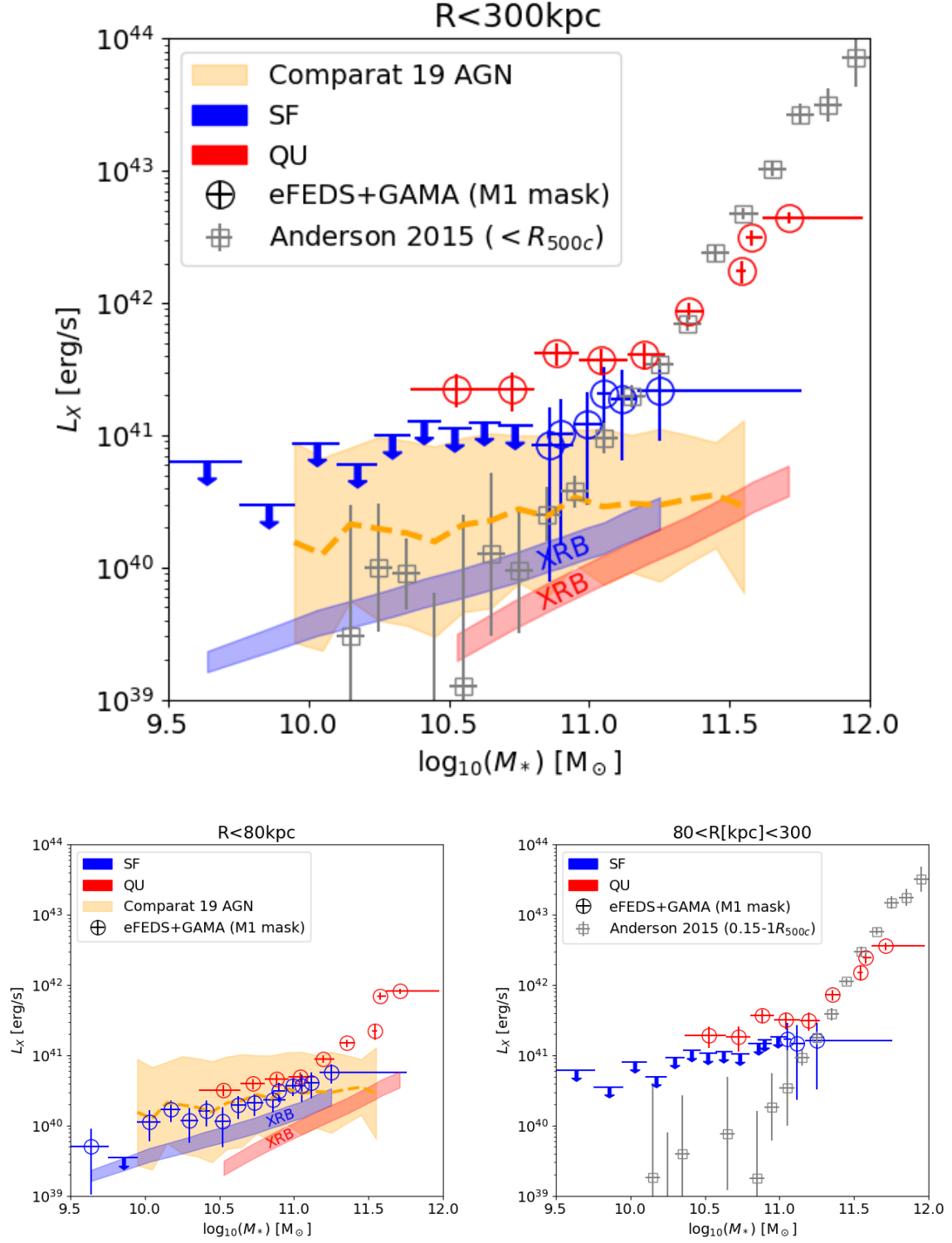


Fig. 10. X-ray 0.5–2 keV projected luminosity around central galaxies as a function of galaxy stellar mass and split into star-forming (blue symbols and annotations) and quiescent (red) samples, computed using the M1 mask. Each eFEDs+GAMA detection is indicated with circles, upper limits with downwards arrows. In the *Main panel*, we show the luminosity integrated within 300 physical projected kpc. In the *Bottom Left Panel*, we show the luminosity integrated within 80 physical projected kpc. In the *Bottom Right Panel*, the relation is shown for the outer shell 80–300 projected kpc. Grey squares are the measurements from [Anderson et al. \(2015\)](#), computed within R_{500c} (main panel) and within $0.15–1 R_{500c}$ (bottom right panel). The orange dashed line and shaded area in the main and bottom left panels shows the prediction from the AGN population synthesis model (after excluding sources with $F_X > 6.5 \times 10^{-15} \text{ erg s}^{-1} \text{ cm}^{-2}$, as per M1 mask) of [Comparat et al. \(2019\)](#), with its uncertainty.

2001) package. There we assume an optically thin plasma in collisional ionisation equilibrium. For elements abundances we em-

ploy the table provided by [Anders & Grevesse \(1989\)](#) re-scaled by the overall metallicity of the gas cells⁶.

⁶ We have checked that, by using the individual abundances of 9 elements tracked by TNG100 instead of the overall metallicity, the X-ray

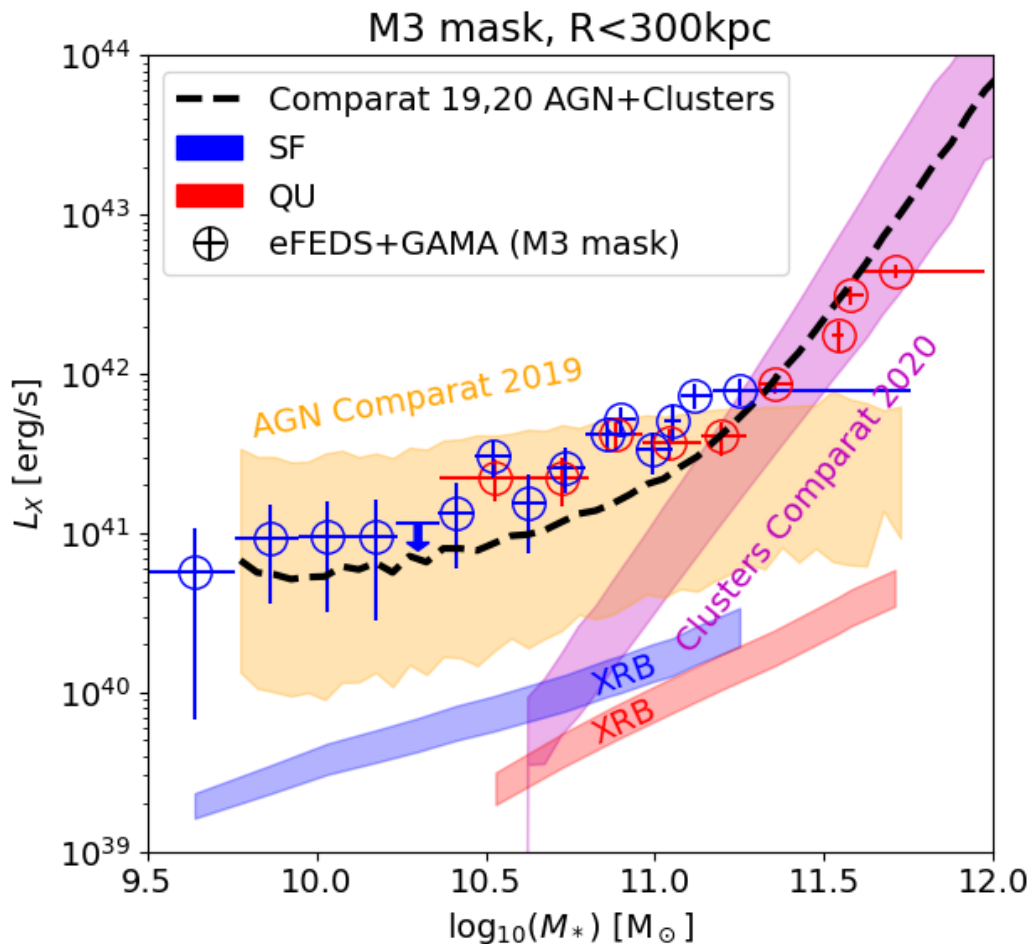


Fig. 11. Same as Fig. 10 for the M3 mask (i.e. including detected point sources). Predictions based on the empirical AGN and cluster models from Comparat et al. (2019, 2020a) (now including sources with $F_X > 6.5 \times 10^{-15} \text{ erg s}^{-1} \text{ cm}^{-2}$, as per M3 mask) are shown as orange (AGN) and purple (groups and clusters) shaded area. The agreement between model and observations is remarkable. For stellar masses between $2 \times 10^{10} M_\odot$ and $2 \times 10^{11} M_\odot$, the positive offset between the observations and models, is likely related to a combination of emission from the CGM and projection effects.

For each TNG100 and EAGLE galaxy matched to the GAMA sample, we sum up the contribution to the total X-ray luminosity along the line of sight in a given projection by accounting for all the gas cells or particles within the Friends-of-Friends selection. To obtain projected X-ray profiles, we take the minimum of the potential as the galaxy center and we determine, for each individual galaxy, the X-ray luminosity as a function of radius in a random projection. We mimic the stacking signal of a specific galaxy sub sample, by taking the average (mean) of the radially-binned X-ray luminosity values from all the simulated galaxies in the matched sub sample. As the eFEDS stacking profiles are de facto weighted by the photon counts in each radial bin, we believe that the *mean* profiles across individual simulated ones is the closest approximation to observed stacked signals.

We convolve the mean simulation profiles with the eROSITA PSF, but we do not remove from the simulation data those unresolved sources that are in fact detected and masked (M1) in the

eFEDS+GAMA results⁷. Moreover, we defer to a future, dedicated paper the task of simulating eROSITA photons as e.g. done for the tailored predictions of Oppenheimer et al. (2020). With such a full forward-modeling into the observational space, we will then also be in the position of replicating, with the simulation data, exactly the stacking procedure adopted here for the eFEDS+GAMA data. This would help in particular to quantify the extent of projection effects along the line of sight.

5.2. Results from IllustrisTNG and EAGLE

Results for the TNG100 and EAGLE galaxies in comparison to eFEDS+GAMA inferences are shown in Figs. 12 and 13, where we focus, respectively, on the projected radial profiles at the transitional mass regime of $5 \times 10^{10} M_\odot$ and on the integrated signal from the CGM as a function of galaxy stellar mass, i.e. integrating the X-ray luminosity between 80 and 300 projected kpc. In both figures, shaded areas around TNG100 results quantify the systematic uncertainties in the sample-matching procedure.

profiles of $5 \times 10^{10} M_\odot$ galaxies vary by about 0.1 dex and overall by negligible amounts in comparison to other systematic uncertainties (as described in Sect. 5.2).

⁷ The latter task requires modelling the X-ray emission not only from the gaseous component but also from AGN and X-ray binaries, which is beyond the scope of the current paper.

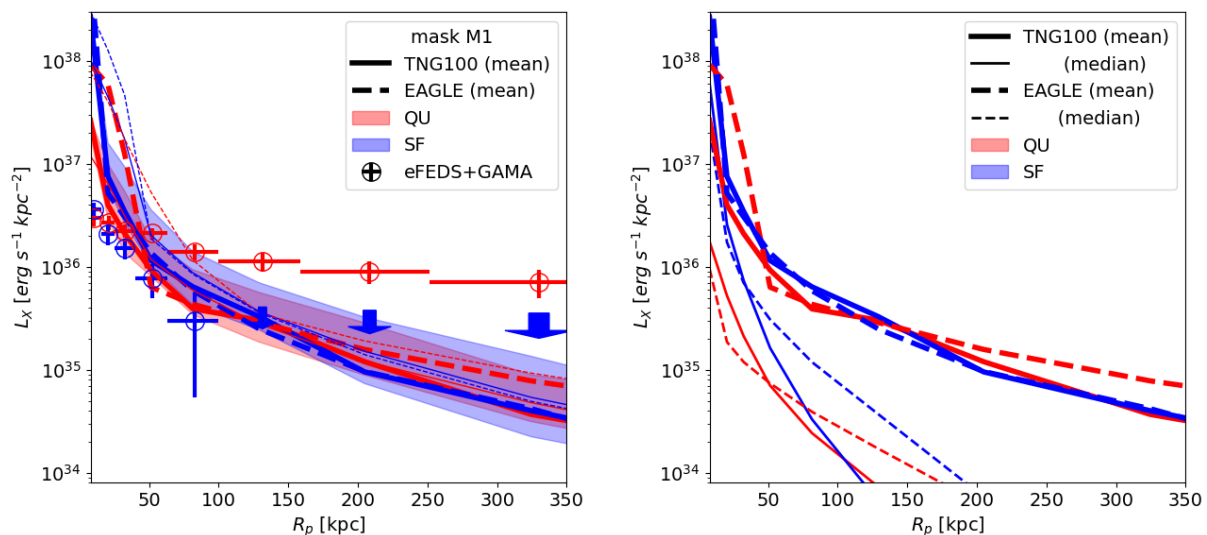


Fig. 12. *Left:* X-ray luminosity projected radial profiles (0.5–2.0 keV rest-frame) for the quiescent QU_M10.7 and the star-forming SF_M10.7 samples (as in Fig. 7 left panel), i.e. for central galaxies with median galaxy stellar mass of about $5 \times 10^{10} M_{\odot}$ and median redshift 0.20. Their mass and redshift distributions is shown in Fig. 5. They are compared to the results from the TNG100 (solid) and the EAGLE (dashed) simulations, consistently matched in stellar mass, sSFR and redshift. Observed stacking results are compared to the mean simulated profiles (thick curves). We convolve the simulated profiles with the PSF and obtain the thin curves. *Right:* complete set of profiles predicted by the simulation: mean (thick), median (thin). The median profiles show where the majority of the simulated profiles are located, it is significantly lower than the mean. Shaded areas represent the systematic uncertainties associated to the extraction of the mocked observable from the simulations (specifically for TNG100) – see text for details.

These are obtained by encompassing the 5th–95th percentile results when: (i) marginalizing over the 20 Monte-Carlo sampling realizations of the GAMA samples; (ii) using the total galaxy stellar masses from the simulations vs. those within smaller apertures: twice half stellar mass radius; (iii) using from the simulations the instantaneous and inner SFR values vs. those averaged over the last 100 Myr. In the profiles of Fig. 12, for example, these systematic choices can amount to X-ray luminosity uncertainties of about 0.5–0.7 dex at 200–300 kpc projected radii.

Comparison between 80 and 300 projected kpc

Focusing on the CGM, at galactocentric distances ≥ 80 kpc, the mean X-ray profiles of MW- and M31-mass galaxies predicted by TNG100 (solid) and EAGLE (dashed curves) are very similar to one another, despite the different underlying galaxy physics models: they both fall within approximately 1 dex from the observational results. In fact, the profiles of the simulated star-forming vs. quiescent galaxies are not significantly different from one another in the simulations, with the simulated X-ray atmospheres around quiescent $10^{10.7} M_{\odot}$ galaxies being less luminous than what the observations imply in Fig. 12.

Figure 13 shows a comparison between the observed extended (between 80 and 300 projected kpc) X-ray luminosity as a function of stellar mass and the simulations’ predictions for the sample matched in redshift, mass and sSFR to the GAMA sample. As for the case of the radial profiles, the CGM luminosity in the soft X-ray band as a function of galaxy stellar mass is not too dissimilar between TNG100 and EAGLE, with similar emission for quiescent and star-forming galaxies at fixed stellar mass in both models.

For the quiescent massive galaxies, TNG100 and EAGLE are in good agreement with the observations, specifically at $\geq 2 \times 10^{11} M_{\odot}$. For $\lesssim 10^{11} M_{\odot}$ galaxies, simulations predict a lower luminosity than observed, consistent with the non-detection of ex-

tended emission around star-forming galaxies, but significantly lower than the observed luminosity of the quiescent galaxies. To note, the simulations predict luminosities possibly larger than that observed by Anderson et al. (2015). The difference between the simulated curves and the observations give a sense of the maximal amount of luminosity that could be imputed to projection effects for quiescent galaxies.

Comparison below 80 projected kpc

It is manifest from Fig. 12 that both TNG100 and EAGLE predict much brighter atmospheres at small galactocentric distances than what found with eFEDS+GAMA: up to two orders of magnitude brighter profiles at < 50 kpc. This is particularly interesting because the simulation signals only come from the volume-filling gas, while in the observations, a part (if not all) of the signal comes from unresolved point sources. This result calls for further investigation.

6. Discussion

The combination of eROSITA’s stable background and good sensitivity at moderate spatial resolution with the availability of a highly complete spectroscopic galaxy sample from GAMA allowed us to detect the faint X-ray emission around galaxies as a function of their measured stellar masses and specific star formation rates.

The work presented here shows a clear dichotomy in the average X-ray emission of star-forming and quiescent galaxies. While the former are only significantly detected on small scales, with a projected luminosity profile consistent with the eROSITA PSF and an intensity compatible with the faint end of the AGN population (with a possible contribution from XRB), the latter show clearly extended projected emission, with increasing intensity for larger stellar masses (at least for $\log_{10} M^* > 11.2$).

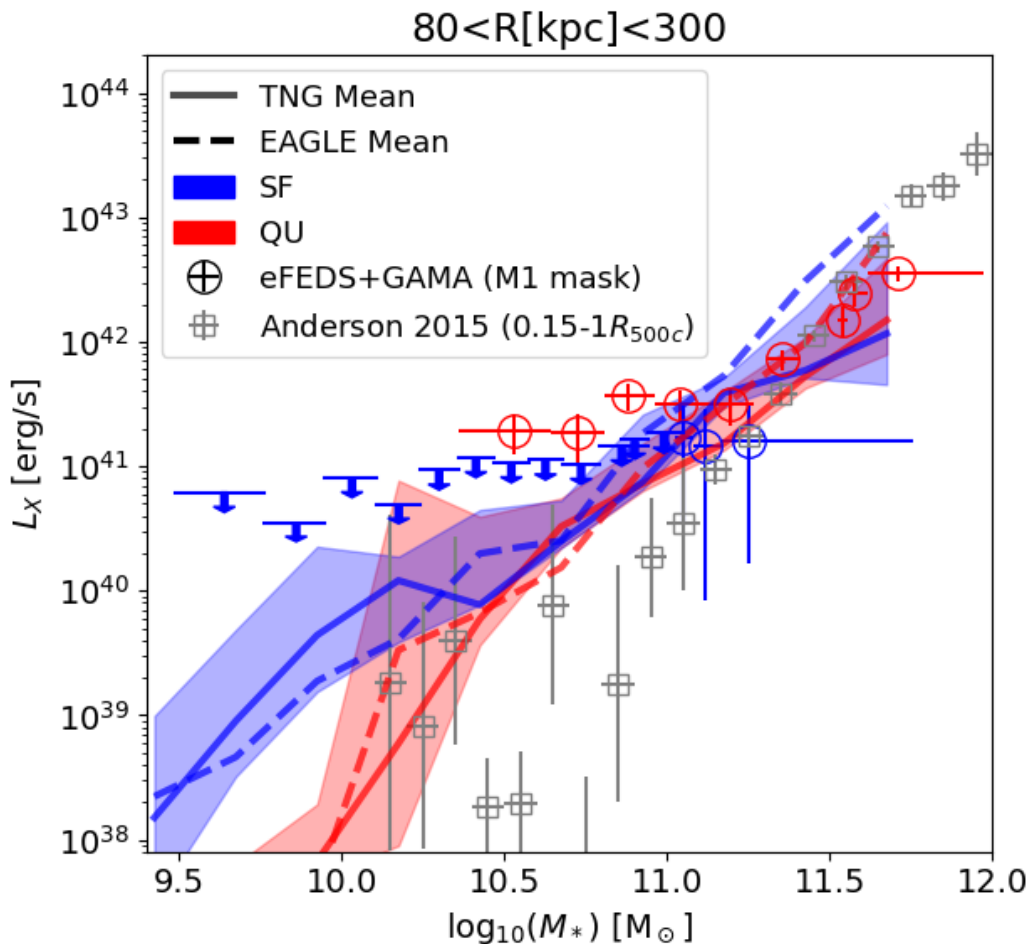


Fig. 13. Same as Fig. 10, bottom right panel, with the addition of the predictions from the TNG100 and EAGLE simulations of matched galaxies. Namely, we show the observed and predicted soft X-ray luminosity from the extended ($80 < R_p < 300$ kpc) CGM around galaxies, as a function of galaxy stellar mass.

In this section, we first discuss possible systematic effects that could affect the interpretations of our results, ranging from the estimate of the contribution from undetected faint AGN or XRB (Sect. 6.1) to the accuracy of the sample selection and the effect of the 2-D projection of the large scale emission surrounding the galaxies (Sect. 6.2). Then, in Sect. 6.3 we move to a discussion of the comparison with the numerical simulations predictions.

6.1. AGN and XRB contamination

The procedure to mask the event files according to a given criterion has a significant impact on the results (see Sect. 4.1). Using ‘ALL’, ‘M1’ or ‘M3’ masks leads to drastically different measurements with distinct physical meanings. In our case, when all resolved sources are identified and classified, the M1 mask is then optimal, as it corresponds to the minimization of contamination from known AGN to the inner projected luminosity profiles. However, the level of residual contamination from undetected faint AGN remains uncertain.

To further estimate the AGN contamination, we use the X-ray AGN model described in Comparat et al. (2019) and validated against eFEDS observations by Teng et al. (2021). We use the X-ray group and cluster model from Comparat et al. (2020a),

which was validated against eFEDS observations by Liu A et al. (2021); Bulbul et al. (2021). In particular they reproduce to good accuracy the number density of sources as a function of their flux ($\log N$ - $\log S$) for each class separately. We limit these light cones to the redshift range $0.05 < z < 0.3$ and flux in the band 0.5–2 keV to $F_X > 10^{-17}$ erg cm $^{-2}$ s $^{-1}$.

We predict as a function of stellar mass the mean luminosity expected for AGN and Clusters, and the scatter around the mean relation. The sum of the two empirical models should correspond to the relation obtained when applying the ‘M3’ mask i.e. when all detected sources are left in the stack. Fig. 11 shows the comparison of the observations with the empirical models. The observations are compatible with the two model lines: at low stellar masses ($\log_{10} M^* < 11.$) the total projected emission of both quiescent and star-forming galaxies must be contaminated by faint AGN⁸. The corresponding contamination from unresolved emission due to X-ray binaries, based on the adopted model for the XRB population in galaxies (see discussion in Sect. 3.2.2; Aird et al. 2017), are reported in the Table 4 (M3 mask) and shown as colored shaded areas in Fig. 11. Clearly, the putative contribution from XRB remain sub-dominant in our stacked sub-samples.

⁸ We note here that the AGN model prediction is in good agreement with the figures from Aird et al. (in prep) quoted in Sect. 3.2.1.

While the comparison with the empirical models provides a reasonable explanation for the observed projected luminosity of both star-forming galaxies (in terms of faint AGN) and high-mass quiescent galaxies (in terms of virialized hot haloes), it does not satisfactorily explain the detection, around low-mass quiescent galaxies, of a significant projected emission well beyond 80 kpc, i.e. much more extended than the potential contamination from purely point sources (see Fig. 3). Additional sources of genuinely extended X-ray emission surrounding those lower-mass quiescent galaxies are likely needed. These may be due to the CGM itself, to an incomplete removal of satellites of luminous clusters and groups, or to projection effects. We discuss these latter two possibilities below.

6.2. Central vs. satellites and projection effects

A well defined central galaxy sample is key to enable the interpretation of our results. With its high completeness, $\sim 98\%$, the GAMA spectroscopic survey allows an accurate distinction between central and satellite galaxies in different environments; the removal of satellite galaxies is then straightforward, and this procedure should not induce systematic effects, provided the GAMA completeness is uniformly high irrespective of environment or galaxy properties. Conversely, we also carried out the same measurements in a sample where satellite galaxies are included and found that the SF profiles remained unchanged, while the QU profiles were systematically 25% brighter at all scales. This is consistent with the fact that on average quiescent satellite galaxies live in hot and dense environments (e.g. [Velander et al. 2014](#)).

The luminosity profiles obtained are subject to projection, similarly to the $w_p(r_p)$ clustering statistics; the environment in which galaxies live has an effect on projected statistics. To investigate its impact, we measure the clustering of the galaxy samples considered, before and after the central selection algorithm is applied, see Fig. 14. In the three dimensional correlation function of the central galaxies sample ($\xi(s)$, top panel, red or blue squares), there is a clear cut-off scale (~ 400 kpc, identified by vertical dashes) below which the clustering signal diminishes, while it is still increasing in the complete sample (centrals plus satellites, red or blue circle). It means that the centrals selection procedure works as expected.

When measuring the projected clustering $w_p(r_p)$, the cut-off scale at ~ 400 kpc is not visible anymore, see Fig. 14, bottom panel. The projected clustering of the full sample and the central sample both extend to very small scales. We see here clearly a projection effect, due to the fact that galaxies live in crowded environments. Therefore, when measuring the projected luminosity profiles, emission around individual galaxies and emission from the environment of the galaxies are mixed up. Both star-forming and quiescent galaxy samples are subject to a similar projection effect, as shown in Fig. 14. However, from the difference seen between the star-forming and quiescent stacked profiles we infer that the environment of $5 \times 10^{10} M_\odot$ (and lower) quiescent galaxies is dense and hot, while that of star-forming galaxies needs to be less dense and cooler. This is in agreement with the findings of [Velander et al. \(2014\)](#). Quantifying accurately the strength of the projection effect and how much it biases the projected luminosity profile as a function of scales is a key to determine how much of the emission measured comes from the CGM. Hopefully future simulations (with full fledged light cones) and further modelling to jointly interpret halo occupation distributions, constrained with clustering and galaxy-galaxy lensing, as well as luminosity profile will shed light on

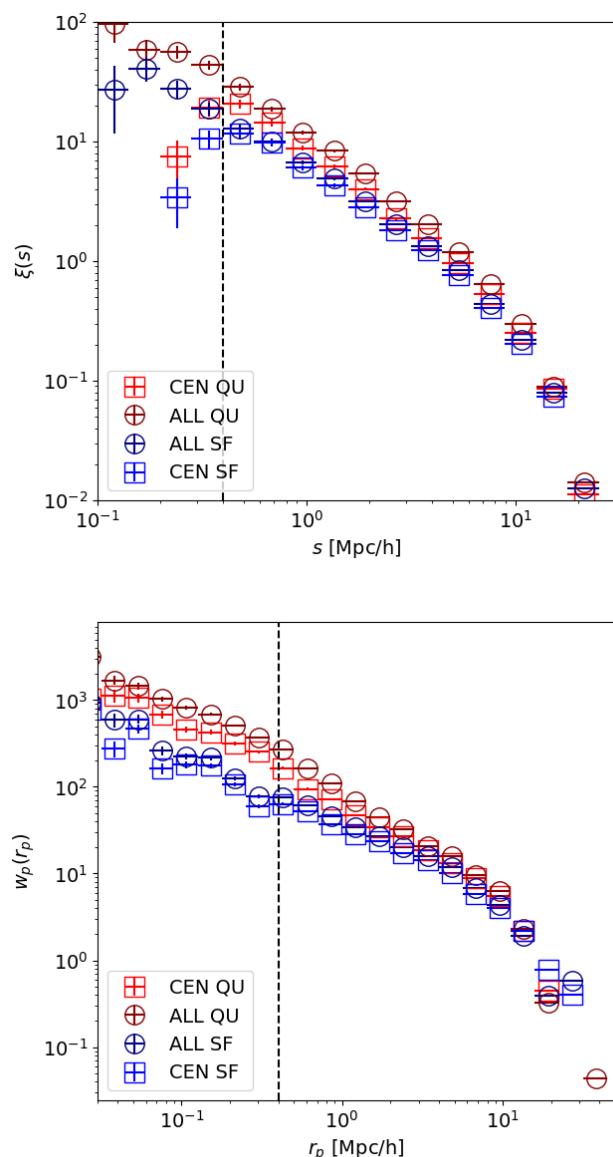


Fig. 14. Clustering of the samples selected. In each panel we show the results for the quiescent central galaxies (CEN QU, red squares), for the star-forming centrals (SF CEN, blue squares), for all the quiescent galaxies (ALL QU, purple circles) and for all the star-forming ones (ALL SF, dark blue circles). *Top Panel:* Three dimensional correlation function. The turn over, illustrated by the vertical dashed line, due to the central selection function is clear. *Bottom Panel:* Projected correlation function: no turnover is visible.

this uncertainty. Because of this, it is unclear if the CGM around $5 \times 10^{10} M_\odot$ galaxies is detected in our sample.

6.3. Insights from the comparison between observations and simulations results

The X-ray profiles and luminosities predicted at large galactocentric distances by TNG100 and EAGLE are in the ball park of the observed ones, and so this allows us to use the simulations to also gather insights that are not achievable otherwise.

It is important to point out that the simulated mean profiles are significantly brighter than the simulated median profiles: see Fig. 12, thick vs. thin solid (TNG100) and dashed (EAGLE)

curves. Conversely, this implies that the CGM signal of the median galaxy is not really captured by the observed mean stacks, which are instead biased high. By analyzing the TNG100 results, we can quantify that the 10 per cent most luminous sources alone can bias high the X-ray signal at ~ 100 kpc by almost 1 dex. This consideration necessitates some caution in the interpretation of the results. Chiefly, given the small volumes considered in this analysis, it is hard to tightly control the population of rare objects in the same manner in the observation and simulations. Samples collected over larger volumes will undoubtedly help addressing this in the future. In the meanwhile, we notice that in TNG100 and EAGLE, no matched galaxy that enters in this analysis lives in a halo more massive than 3×10^{13} – $10^{14} M_{\odot}$, throughout the whole sample and even though more massive haloes are present in the simulated volumes. On the other hand, there are at least (X-ray detected) 289 galaxy clusters and groups in the 60 deg^2 of eFEDS and GAMA (Liu A et al. 2021).

Also, when comparing results from the two simulations, TNG100 and EAGLE, we find overall very consistent mean profiles whereas median profiles differ. The median discrepancy is related to the different underlying galaxy physics models of the simulations. This highlights the fact that the median profiles are sensitive to the galaxy evolution model, while the mean profiles are more sensitive to a sparse population of rare and luminous galaxies. For example, at the transitional mass regime of Fig. 12, it is evident that EAGLE atmospheres are X-ray brighter than TNG ones, consistently with the notion that the SMBH feedback in TNG is more ejective than in EAGLE (Davies et al. 2020; Truong et al. 2021) and that EAGLE exhibits lower quiescent fractions than TNG at this mass scale (Donnari et al. 2021).

At face value, the X-ray luminosity of the CGM around $10^{10.2}$ – $10^{10.8} M_{\odot}$ star-forming galaxies are consistent with the upper limits inferred from eFEDS+GAMA data. The simulation results are suggestive that a detection of the hot CGM around star-forming MW/M31-mass galaxies may not be far (see Sect. 7).

Importantly, it is also apparent from both Figs. 12 and 13 that TNG100 and EAGLE do not predict a significant difference in the CGM X-ray signals between quiescent and star-forming galaxies, as seen in the data. Instead, the mean profiles and the CGM luminosities on large scales from the simulations fall closer to the observed SF eROSITA results. This is likely due to the aforementioned projection effects.

Also, it should be noted that these results are not necessarily in contradiction with results reported in the introduction, i.e. of brighter X-ray atmospheres around simulated star-forming galaxies than around quiescent ones (Truong et al. 2020; Oppenheimer et al. 2020). Firstly, here we are comparing mean profiles and not median properties of galaxies; secondly, here we focus on somewhat higher redshift, $z \sim 0.2$ vs. $z \sim 0.1$; and finally, the stacked profiles of Figure 12 are not from volume-limited samples and reflect the mean results of galaxies in rather wide mass and redshift bins and with different stellar mass and redshift distributions in the two star-forming and quiescent bins, with the former exhibiting a relative higher representation of lower-mass and higher-redshift galaxies (see Fig. 5).

As pointed out earlier, for more accurate comparisons between observations and simulations, a more thorough forward model of the simulation data would be needed, e.g. by using *sixte* (Dauser et al. 2019). However, focusing on the discrepancy at face value for the $5 \times 10^{10} M_{\odot}$ quiescent galaxies (Fig. 12), we can argue that under-luminous atmospheres in the simulations in comparison to data may indicate that (some of the) simulated gaseous haloes may a) be under-dense, b) be characterized by lower temperatures, and/or c) be less enriched than

(some of the) galaxies in the Universe, or more specifically in eFEDS. This in turn could be due to a SMBH feedback implementation that is too ejective than in reality, at least in some cases – more ejective SMBH feedback would imply more substantial outflows and hence a more substantial clearing of the halo, of both hot and metal-enriched gas – or that is not effective enough at heating up the halo gas.

7. Summary and outlook

We have quantified the X-ray emission around a large sample of quiescent (star-forming) galaxies at $0.05 < z < 0.3$ in the stellar mass range $2 \times 10^{10} - 10^{12} M_{\odot}$ ($3 \times 10^9 - 6 \times 10^{11} M_{\odot}$) (Fig. 1). To do so, we have stacked the eROSITA eFEDS events around central GAMA galaxies to obtain projected luminosity profiles out to hundreds of project kpc (Figs. 4, 6, 7, 8, 9). As anticipated, the stacking method is successful to overcome the flux limit in the X-ray observations⁹.

For quiescent (passive) galaxies, the X-ray profiles are clearly extended throughout the available mass range (e.g. Fig. 7); however, the measured profiles are likely biased high due to projection effects emanating from the fact that quiescent galaxies live in dense and hot environments (Fig. 14). Around star-forming galaxies with $< 10^{11} M_{\odot}$, the X-ray stacked profiles are compatible with unresolved sources and consistent with the expected emission from faint active galactic nuclei and X-ray binaries (Fig. 7). Only for the most massive star forming samples ($\geq 10^{11} M_{\odot}$), there is a hint of detection of extended emission.

We measure for the first time the average relation between mean projected X-ray luminosity within various apertures and stellar mass separately for quiescent and star-forming galaxies (Fig. 10). We find that the relation is different for the two galaxy populations: high-mass ($\geq 10^{11} M_{\odot}$) star-forming or quiescent galaxies follow the expected scaling of virialized hot haloes. Lower mass star-forming galaxies show a less prominent luminosity and a weaker dependence on stellar mass, consistent with empirical models of the population of weak AGN.

In particular, when measuring the mean projected X-ray luminosity in a 300 kpc aperture while excluding point sources (M1 mask, Fig. 10 main panel and Table 3), for quiescent galaxies with a stellar mass larger than $2 \times 10^{10} M_{\odot}$, we detect (signal to noise larger than 3) a faint X-ray emission partly originating from hot gas. For star-forming galaxies with a stellar mass larger than $6 \times 10^{10} M_{\odot}$, we report a hint of detection (signal to noise between 1 and 3). For star-forming galaxies with a stellar mass in the range 3×10^9 – $6 \times 10^{10} M_{\odot}$ we measure upper limits (signal to noise smaller than 1). We find similar results and detection levels when we measure the average projected X-ray luminosity in a 80–300 kpc aperture (M1 mask, Fig. 10 bottom right panel and Table 3), which hence characterize the extended emission beyond the galaxy itself: we detect X-ray extended emission around quiescent galaxies at all probed masses, while for star-forming galaxies we find upper limits in the 3×10^9 – $10^{11} M_{\odot}$ range and a hint of detection at higher masses.

We additionally measure the average projected X-ray luminosity in a 300 kpc aperture while keeping all detected point sources (M3 mask, Fig. 11 and Table 4). We find good agreement with empirical models of the X-ray cosmic web of AGN and clusters from Comparat et al. (2019, 2020a). This reinforces

⁹ For example, the QU_M10.53 sample, with a signal to noise of about 5.5, has a luminosity in the inner 80 kpc of $3.2 \times 10^{40} \text{ erg s}^{-1}$ at redshift 0.19, corresponding to a flux of $3.1 \times 10^{-16} \text{ erg cm}^{-2} \text{ s}^{-1}$. This is about 20 times fainter than the flux limit of quoted by Brunner et al. (2021).

Table 5. Signal to noise forecast for future eROSITA-based experiments.

	Area [deg ²]	N_g [10 ⁶]	$\langle \frac{t_{\text{exp}}}{t_{\text{exp,eFEDS}}} \rangle$	ξ_{SNR}
eRASS1 + public 2021	21k	1.2	0.1	1.8
eRASS:8 + WAVES	1k	0.7	0.8	4.0
eRASS:3 + DESI BGS	5k	7	0.3	7.7
eRASS:8 ‘Legacy’	21k	20	0.8	21.2

Notes. Average signal to noise improvement ratio with respect to the eFEDS+GAMA09 sample (ξ_{SNR}) for four possible combination of eROSITA all-sky survey depths and low-redshift galaxy spectroscopic samples. The Area (in square degrees) reported is the approximate overlap between the German eROSITA all-sky survey (Sunyaev et al. 2021) and the galaxy samples; N_g is the number of galaxies with $z \lesssim 0.3$ in this area (in millions), while $\langle \frac{t_{\text{exp}}}{t_{\text{exp,eFEDS}}} \rangle$ is the average ratio between the corresponding eRASS exposure and the eFEDS one.

the notion that a robust assessment of the properties of hot haloes in Milky-Way-like galaxies (and smaller) requires an accurate removal of AGN contaminants.

When comparing our results with state-of-the art numerical simulations (IllustrisTNG and EAGLE), we find an overall consistency on the average emission on large (> 80 kpc) scales at masses $\geq 10^{11} M_{\odot}$, but disagreement on the small scales, where brighter than observed compact cores are predicted (Fig. 12). The simulations also do not predict the clear differentiation that we observe between quiescent and star-forming galaxies in our samples (Fig. 13).

This work is a stepping stone towards a better understanding of the hot phase in the circum-galactic medium, which holds a key role in the regulation of star formation. In the next decade, by combining eROSITA with upcoming spectroscopic galaxy surveys (e.g. DESI, SDSS-V, 4MOST: DESI Collaboration et al. 2016; Kollmeier et al. 2017; de Jong et al. 2019; Merloni et al. 2019; Finoguenov et al. 2019), properties of the CGM and their relation to active galactic nuclei should be unraveled. The eROSITA all-sky survey (eRASS) data cover more than hundred times more extra-galactic sky than eFEDS and therefore offer the opportunity to improve on the analysis presented here.

In Table 5 we provide a rough estimate of the average signal to noise ratio improvement ratio (ξ_{SNR}), based on a full-sample, for a few selected combinations of different eRASS depths (from the single-pass eRASS1 to the full eight-passes eRASS:8) and extra-galactic spectroscopic surveys. We assume, for simplicity, that $\text{SNR} \propto \sqrt{N_g t_{\text{exp}}}$, where N_g is the number of galaxies in the range $z \lesssim 0.3$ and t_{exp} is the average eROSITA exposure. We compute the ratio of the SNR, ξ_{SNR} , obtainable with these experiments to the eFEDS+GAMA09 baseline one, for which we take $N_{g,eFEDS} = 35,521$. We provide estimates for the following combinations:

- eRASS1 with a compilation of existing spectroscopic catalogues (‘eRASS1 + public 2021’);
- An intermediate stage that combines a three-passes X-ray survey (eRASS:3) with the DESI ‘Bright Galaxy Survey’ (BGS, Ruiz-Macias et al. 2020);
- The full-depth eRASS:8 combined with the 4MOST WAVES wide survey (Driver et al. 2016);
- A putative ‘Legacy’ sample, combining eRASS:8 with all spectroscopic samples available in about a decade (early 2030s).

The average signal to noise improvement with respect to the sample analysed here range from about a factor of 1.8 to more than a factor of 20. Further improvements in the eROSITA data processing, energy and PSF calibration, will likely also increase the significance of the detection, and enable a combination of spatial and spectral analysis. Thanks to those improvements, we should be able to measure the temperature and metallicity of the hot CGM, as well as its density and pressure profile. Hopefully, this will shed light on how hot haloes are created and energized, and their interplay with the star formation and virialization processes, as well as feedback processes from active galactic nuclei.

Acknowledgements. This work is based on data from eROSITA, the soft X-ray instrument aboard *SRG*, a joint Russian-German science mission supported by the Russian Space Agency (Roskosmos), in the interests of the Russian Academy of Sciences represented by its Space Research Institute (IKI), and the Deutsches Zentrum für Luft- und Raumfahrt (DLR). The *SRG* spacecraft was built by Lavochkin Association (NPOL) and its subcontractors, and is operated by NPOL with support from the Max Planck Institute for Extraterrestrial Physics (MPE). The development and construction of the eROSITA X-ray instrument was led by MPE, with contributions from the Dr. Karl Remeis Observatory Bamberg & ECAP (FAU Erlangen-Nürnberg), the University of Hamburg Observatory, the Leibniz Institute for Astrophysics Potsdam (AIP), and the Institute for Astronomy and Astrophysics of the University of Tübingen, with the support of DLR and the Max Planck Society. The Argelander Institute for Astronomy of the University of Bonn and the Ludwig Maximilians Universität Munich also participated in the science preparation for eROSITA. The eROSITA data shown here were processed using the eSASS software system developed by the German eROSITA consortium. GAMA is a joint European-Australasian project based around a spectroscopic campaign using the Anglo-Australian Telescope. The GAMA input catalogue is based on data taken from the Sloan Digital Sky Survey and the UKIRT Infrared Deep Sky Survey. Complementary imaging of the GAMA regions is being obtained by a number of independent survey programmes including GALEX MIS, VST KiDS, VISTA VIKING, WISE, Herschel-ATLAS, GMRT and ASKAP providing UV to radio coverage. GAMA is funded by the STFC (UK), the ARC (Australia), the AAO, and the participating institutions. The GAMA website is <http://www.gama-survey.org/>. This project acknowledges funding from the European Research Council (ERC) under the European Union’s Horizon 2020 research and innovation programme (grant agreement No 865637).

References

- Ahumada, R., Prieto, C. A., Almeida, A., et al. 2020, *ApJS*, 249, 3
 Aird, J., Coil, A. L., & Georgakakis, A. 2017, *MNRAS*, 465, 3390
 Anders, E. & Grevesse, N. 1989, *Geochim. Cosmochim. Acta*, 53, 197
 Anderson, M. E., Churazov, E., & Bregman, J. N. 2016, *MNRAS*, 455, 227
 Anderson, M. E., Gaspari, M., White, S. D. M., Wang, W., & Dai, X. 2015, *MNRAS*, 449, 3806
 Bahar, Y. E., Bulbul, E., Clerc, N., et al. 2021, arXiv e-prints, arXiv:2110.09534
 Baldry, I. K., Robotham, A. S. G., Hill, D. T., et al. 2010, *MNRAS*, 404, 86
 Barnes, D. J., Kay, S. T., Bahé, Y. M., et al. 2017, *MNRAS*, 471, 1088
 Basu-Zych, A. R., Hornschemeier, A. E., Haberl, F., et al. 2020, *MNRAS*, 498, 1651
 Behroozi, P., Wechsler, R. H., Hearin, A. P., & Conroy, C. 2019, *MNRAS*, 488, 3143
 Behroozi, P. S., Wechsler, R. H., & Conroy, C. 2013, *ApJ*, 770, 57
 Bellstedt, S., Robotham, A. S. G., Driver, S. P., et al. 2021, *MNRAS*, 503, 3309
 Bellstedt, S., Robotham, A. S. G., Driver, S. P., et al. 2020, *MNRAS*, 498, 5581
 Bogdán, Á., Bourdin, H., Forman, W. R., et al. 2017, *ApJ*, 850, 98
 Bogdán, Á., Forman, W. R., Kraft, R. P., & Jones, C. 2013a, *ApJ*, 772, 98
 Bogdán, Á., Forman, W. R., Vogelsberger, M., et al. 2013b, *ApJ*, 772, 97
 Bogdán, Á., Vogelsberger, M., Kraft, R. P., et al. 2015, *ApJ*, 804, 72
 Bregman, J. N., Anderson, M. E., Miller, M. J., et al. 2018, 862, 3
 Brunner, H., Liu, T., Lamer, G., et al. 2021, arXiv e-prints, arXiv:2106.14517
 Bulbul, E., Liu, A., Pasini, T., et al. 2021, arXiv e-prints, arXiv:2110.09544
 Churazov, E., Khabibullin, I., Lyskova, N., Sunyaev, R., & Bykov, A. M. 2020, arXiv e-prints, arXiv:2012.11627
 Comparat, J., Eckert, D., Finoguenov, A., et al. 2020a, *The Open Journal of Astrophysics*, 3, 13
 Comparat, J., Merloni, A., Dwelly, T., et al. 2020b, *A&A*, 636, A97
 Comparat, J., Merloni, A., Salvato, M., et al. 2019, *MNRAS*, 487, 2005
 Crain, R. A., McCarthy, I. G., Frenk, C. S., Theuns, T., & Schaye, J. 2010, *MNRAS*, 407, 1403
 Crain, R. A., Schaye, J., Bower, R. G., et al. 2015, *MNRAS*, 450, 1937

Dauser, T., Falkner, S., Lorenz, M., et al. 2019, *A&A*, 630, A66

Davies, J. J., Crain, R. A., Oppenheimer, B. D., & Schaye, J. 2020, *MNRAS*, 491, 4462

Davies, L. J. M., Lagos, C. d. P., Katsianis, A., et al. 2019, *MNRAS*, 483, 1881

de Jong, R. S., Agertz, O., Berbel, A. A., et al. 2019, *The Messenger*, 175, 3

DESI Collaboration, Aghamousa, A., Aguilar, J., et al. 2016, arXiv e-prints, arXiv:1611.00036

Donnari, M., Pillepich, A., Nelson, D., et al. 2021, *MNRAS*, 506, 4760

Driver, S. 2021, *Nature Astronomy*, 5, 852

Driver, S. P., Davies, L. J., Meyer, M., et al. 2016, in *Astrophysics and Space Science Proceedings*, Vol. 42, *The Universe of Digital Sky Surveys*, ed. N. R. Napolitano, G. Longo, M. Marconi, M. Paolillo, & E. Iodice, 205

Finoguenov, A., Merloni, A., Comparat, J., et al. 2019, *The Messenger*, 175, 39

Fukugita, M. & Peebles, P. J. E. 2004, *ApJ*, 616, 643

Fukugita, M. & Peebles, P. J. E. 2006, *ApJ*, 639, 590

Georgakakis, A., Comparat, J., Merloni, A., et al. 2019, *MNRAS*, 487, 275

Georgakakis, A., Nandra, K., Laird, E. S., Aird, J., & Trichas, M. 2008, *MNRAS*, 388, 1205

Goulding, A. D., Greene, J. E., Ma, C.-P., et al. 2016, *ApJ*, 826, 167

Ilbert, O., McCracken, H. J., Le Fèvre, O., et al. 2013, *A&A*, 556, A55

Kelly, A. J., Jenkins, A., & Frenk, C. S. 2021, *MNRAS*, 502, 2934

Kollmeier, J. A., Zasowski, G., Rix, H.-W., et al. 2017, arXiv e-prints, arXiv:1711.03234

Lehmer, B. D., Basu-Zych, A. R., Mineo, S., et al. 2016, *ApJ*, 825, 7

Li, J.-T., Bregman, J. N., Wang, Q. D., Crain, R. A., & Anderson, M. E. 2016, *ApJ*, 830, 134

Liske, J., Baldry, I. K., Driver, S. P., et al. 2015, *MNRAS*, 452, 2087

Liu A, Bulbul, E., Ghirardini, V., et al. 2021, arXiv e-prints, arXiv:2106.14518

Liu T, Buchner, J., Nandra, K., et al. 2021, arXiv e-prints, arXiv:2106.14522

Lovisari, L., Reiprich, T. H., & Schellenberger, G. 2015, *A&A*, 573, A118

Marinacci, F., Vogelsberger, M., Pakmor, R., et al. 2018, *MNRAS*, 480, 5113

McAlpine, S., Helly, J. C., Schaller, M., et al. 2016, *Astronomy and Computing*, 15, 72

Mehrtens, N., Romer, A. K., Hilton, M., et al. 2012, *MNRAS*, 423, 1024

Merloni, A., Alexander, D. A., Banerji, M., et al. 2019, *The Messenger*, 175, 42

Moster, B. P., Naab, T., & White, S. D. M. 2013, *MNRAS*, 428, 3121

Moster, B. P., Naab, T., & White, S. D. M. 2018, *MNRAS*, 477, 1822

Naiman, J. P., Pillepich, A., Springel, V., et al. 2018, *MNRAS*, 477, 1206

Nelson, D., Pillepich, A., Springel, V., et al. 2018, *MNRAS*, 475, 624

Nelson, D., Springel, V., Pillepich, A., et al. 2019, *Computational Astrophysics and Cosmology*, 6, 2

Oppenheimer, B. D., Bogdán, Á., Crain, R. A., et al. 2020, *ApJ*, 893, L24

Pillepich, A., Nelson, D., Hernquist, L., et al. 2018, *MNRAS*, 475, 648

Planck Collaboration, Ade, P. A. R., Aghanim, N., et al. 2013, *A&A*, 557, A52

Planck Collaboration, Ade, P. A. R., Aghanim, N., et al. 2016, *A&A*, 594, A24

Popesso, P., Magnelli, B., Buttiglione, S., et al. 2012, arXiv e-prints, arXiv:1211.4257

Pratt, G. W., Croston, J. H., Arnaud, M., & Böhringer, H. 2009, *A&A*, 498, 361

Predehl, P., Andritschke, R., Arefiev, V., et al. 2021, *A&A*, 647, A1

Robotham, A. S. G., Bellstedt, S., Lagos, C. d. P., et al. 2020, *MNRAS*, 495, 905

Ruiz-Macias, O., Zarrouk, P., Cole, S., et al. 2020, *Research Notes of the American Astronomical Society*, 4, 187

Salvato, M., Wolf, J., Dwelly, T., et al. 2021, arXiv e-prints, arXiv:2106.14520

Schaye, J., Crain, R. A., Bower, R. G., et al. 2015, *MNRAS*, 446, 521

Smith, R. K., Brickhouse, N. S., Liedahl, D. A., & Raymond, J. C. 2001, *ApJ*, 556, L91

Springel, V., Pakmor, R., Pillepich, A., et al. 2018, *MNRAS*, 475, 676

Sun, M. 2012, *New Journal of Physics*, 14, 045004

Sunyaev, R., Arefiev, V., Babyshkin, V., et al. 2021, arXiv e-prints, arXiv:2104.13267

Tauris, T. M. & van den Heuvel, E. P. J. 2006, *Formation and evolution of compact stellar X-ray sources*, Vol. 39, 623–665

Teng, L., Merloni, A., Comparat, J., et al. 2021, arXiv e-prints, arXiv:2106.14528

Thorne, J. E., Robotham, A. S. G., Davies, L. J. M., et al. 2021, *MNRAS*, 505, 540

Truong, N., Pillepich, A., Nelson, D., Werner, N., & Hernquist, L. 2021, *MNRAS*, 508, 1563

Truong, N., Pillepich, A., Werner, N., et al. 2020, *MNRAS*[arXiv:1911.11165]

Tumlinson, J., Peebles, M. S., & Werk, J. K. 2017, *ARA&A*, 55, 389

Velander, M., van Uitert, E., Hoekstra, H., et al. 2014, *MNRAS*, 437, 2111

Vikhlinin, A., Burenin, R. A., Ebeling, H., et al. 2009, *ApJ*, 692, 1033

Vulic, N., Hornschemeier, A. E., Haberl, F., et al. 2021, arXiv e-prints, arXiv:2106.14526

White, S. D. M. & Frenk, C. S. 1991, *ApJ*, 379, 52

Wolf, J., Salvato, M., Coffey, D., et al. 2020, *MNRAS*, 492, 3580

Zhu, G. B., Comparat, J., Kneib, J.-P., et al. 2015, *ApJ*, 815, 48

Appendix A. Matching procedure between simulated and observed galaxy samples

It is complex to directly compare the results of the simulations e.g. from [Truong et al. 2020](#) and [Oppenheimer et al. 2020](#) to those from our observations because, as a start, they are given at different redshifts ($z \sim 0$ vs. median $z \sim 0.2$), which correspond to a 2.5 Gyr difference in the age of the Universe. Secondly, the galaxy samples from the simulations at any given epoch are volume limited whereas those in GAMA are magnitude limited, with progressively larger fractions of more luminous and massive galaxies at higher redshifts (see [Figure 1](#)).

We hence construct simulated galaxy samples that are matched to the observed ones by finding, for each galaxy in the GAMA set, its simulated equivalent in TNG and EAGLE. We use simulated data from the TNG100 and Ref-L0100N1504 runs, which both encompass approximately 100 comoving Mpc a side. We consider only central galaxies, in line with the choices of [Sect. 3.1](#). However, we do not replicate the methods adopted for the observed data, but simply identify as centrals those galaxies that occupy the lowest level of the gravitational potential of the simulated haloes identified with the Friends-of-Friends algorithm. In TNG, we exclude objects with `SubhaloFlag` $\equiv 0$ (see [Nelson et al. 2019](#), for more details). The analog objects between the simulation outputs and the GAMA sample are found in the redshift, galaxy stellar mass, and sSFR parameter space.

The match in redshift is done to the closest available simulation snapshot. In the $0.05 < z < 0.3$ range considered here, there are 18 data snapshots in TNG and 3 in EAGLE.

As a fiducial choice, we assume that the stellar mass of GAMA galaxies inferred by [Bellstedt et al. \(2020, 2021\)](#) are close to the total mass of a galaxy, i.e. is compatible with the sum of all the stellar particles that are gravitationally-bound to a simulated galaxy. However, this is probably not the case for centrals in massive haloes and so we bracket this uncertainty by also matching the samples assuming that the GAMA stellar masses correspond to the sum of the stellar particles that are gravitationally-bound to a simulated galaxy and within twice its stellar half-mass radius.

We also assume that the inferred SFR of the observed galaxies is equivalent to the instantaneous SFR of the gas cells of a simulated galaxy, again within twice its stellar half-mass radius. In fact, GAMA’s SFRs are averaged over 100 Myr: as shown by [Donnari et al. 2021](#), at least for TNG, whether SFRs are de facto instantaneous vs. averaged across the past 1 Gyr and whether they are measured across varying galaxy apertures should not be important for the main purposes of this paper, i.e. for splitting galaxies into quiescent and star-forming ones at low z and as long as the rule for the grouping is the same – see below. However, even within the quiescent and star-forming samples, the X-ray CGM signal may in fact show trends with the actual level of SFR, and hence we also show results adopting 100 Myr-averaged values measured throughout the galaxy body. We manually re-label sSFR values below 10^{-15} yr^{-1} to exactly 10^{-15} yr^{-1} , in both observation and simulations data, to avoid being affected by highly-uncertain or numerical resolution-dependent SFR estimations.

For every GAMA galaxy at a given redshift (see [Table 1](#)), a simulated analog is searched for in the stellar mass – sSFR plane at the closest snapshot by randomly selecting a galaxy within a rectangle whose widths are equivalent to the uncertainties associated to the measured values of stellar mass and SFR on a galaxy-by-galaxy basis. If no simulated galaxy is found within such limits, we simply take the closest simulated galaxy to the

observed one – this occurs only for ~ 400 (~ 800) GAMA galaxies when matching to TNG (EAGLE). We repeat this procedure for the overall sample 20 times for both TNG and EAGLE, so to obtain 20 different Monte Carlo simulation samples matched to the observational ones.

Quiescent and star-forming matched simulated galaxies are then divided with the fixed boundary cut at $\log_{10}(\text{sSFR}) = -11$, as in Sect. 2.2. Bins in galaxy stellar mass as described in Table 1 are extracted from the overall matched samples.

As the TNG and EAGLE volumes ($\sim 10^6 \text{ Mpc}^3$) are smaller than that of the galaxy sample considered here ($\sim 10^7 \text{ Mpc}^3$), the same simulated galaxies may be matched to multiple observed galaxies. In these cases, the direction from which the galaxy is seen (when projected on sky) is changed to avoid repetitions of the exact same X-ray profiles when simulating the stacking procedure. In the matched TNG100 samples, about 30% of the objects come from simulated galaxies that are not unique. This fraction increases to 43% for galaxies $M^* > 10^{11} M_{\odot}$.